Available online at www.sciencedirect.com
ScienceDirect
Comput. Methods Appl. Mech. Engrg. 417 (2023) 116361
Computer methods in applied mechanics and engineering
www.elsevier.com/locate/cma

# A variationally consistent contact formulation based on a mixed interpolation point method and isogeometric discretization

Thang X. Duong[a], Leonardo Leonetti[b], Josef Kiendl[a,*]

[a] University of the Bundeswehr Munich, Werner-Heisenberg-Weg 39, 85577 Neubiberg, Germany
[b] University of Calabria, Via Pietro Bucci, 87036 Rende CS, Italy

Available online 26 August 2023

**Abstract**

This work enhances the robustness of the standard displacement-based (penalty Gauss-point-to-segment) contact formulation by applying the so-called Mixed Interpolation Point method (MIP). We consider a smooth isogeometric discretization of the contact surface in order to avoid various artificial discontinuities of the normal contact gap function. Like any existing MIP-enhanced formulation in terms of implementation, the proposed MIP contact formulation only requires a minor modification from an existing implementation of the standard contact formulation. Nevertheless, the improvement in robustness is shown to be quite significant, which often enables the simulation of contact problems with a larger load step size for efficiency and/or a larger penalty parameter for accuracy in the contact constraint. The formalism of the proposed MIP contact method is based on the idea of relaxing the contact constitution at integration points. To this end, at first the contact pressure is considered as an additional unknown apart from the displacement field, and the perturbed Lagrange multiplier potential is used to enforce the contact constraint. The MIP method then eliminates the contact pressure unknown directly at integration points, instead of discretizing it as it is done in the standard mixed contact formulations. As a result, the residual vector is identical to the standard displacement-based contact formulation. However, the resulting tangent stiffness matrix is different, as the MIP tangent is now based on an extrapolation of the contact pressure iteratively over Newton iterations. Several challenging numerical examples are presented to illustrate the accuracy, robustness and efficiency of the proposed formulation.


*Keywords:* Mixed interpolation; Isogeometric analysis; Mortar method; Contact formulation

## 1. Introduction

This paper is dedicated to Dr. Thomas J.R. Hughes and his lifetime achievements in the field of computational mechanics. His visionary idea of isogeometric analysis has been a driving inspiration for all the authors of this paper throughout their careers and also laid the basis for their joint work in this paper.

Concerning about the finite element method for contact problems, assuring the robustness and accuracy of the underlying contact algorithm is not trivial in a general contact scenario, which can involve large deformation, large contact sliding, geometrical and material nonlinearities, and structural and material instabilities. These factors may directly or indirectly lead to a divergence of a contact computation. A cause of divergence is usually rooted in the

* Corresponding author.
*E-mail address:* josef.kiendl@unibw.de (J. Kiendl).

https://doi.org/10.1016/j.cma.2023.116361

existence of various discontinuities within the discretized contact surface, such as discontinuities of the geometrical contact surface itself and/or discontinuities of the contact gap (or the contact pressure) [1]. These discontinuities can be either *artificial discontinuities*, e.g. at element boundaries when the contact surface is discretized by classical Lagrange elements. Or they can be *physical discontinuities*, e.g. at the edges of contact bodies. In any case, such discontinuities lead to a discontinuous (point-wise) contact gap function, which is often used to enforce the impenetrability contact condition. Consequently, it may cause many divergent-related issues, such as a geometrical locking in the context of large sliding contacts, or inaccuracy in the numerical surface integration over the contact surface.

In recent decades, computational contact mechanics made advancements in terms of robustness mainly due to the advent of (i) mortar methods [2] – see e.g. Puso and Laursen [3] for a pioneering work in mortar contact, and (ii) isogeometric analysis [4] – see e.g. Lu [5], Temizer et al. [6], and De Lorenzis et al. [7] for pioneers in the context of isogeometric contact. Both mortar methods and isogeometric contact aim at tackling the above-mentioned discontinuities for improving robustness, but in different ways.

In mortar methods, a smoothed contact gap (or weighted contact gap) is enforced for the impenetrability contact condition, instead of the point-wise contact gap with the above-mentioned discontinuities. In other words, the contact constraint is reformulated in a weak sense, see e.g. [8,9]. This approach helps to overcome the geometrical interlocking issue [10]. A shortcoming of the method, however, is the appearance of new artificial discontinuities at the overlapping boundaries of slave and master elements of the finite element force terms acting on master elements. Such discontinuities still appear even with the novel smooth isogeometric discretization technique and usually require a segmentation procedure in order to resolve the numerical integration there [1]. Apart from artificial discontinuities within a contact zone, a proper segmentation helps to resolve physical discontinuities at the edges of contact bodies as well [11]. Despite the burden of segmentation, improvement of the robustness in mortar methods is significant, and it becomes widely used in contact simulations [12–15].

Isogeometric contact, on the other hand, improves the robustness by providing a smooth discretization of contact surfaces, which eliminates many issues related to artificial discontinuities of the point-wise contact gap. Therefore, the robustness is shown – by e.g. [16,17] – to be significantly improved even with the classical constraint enforcement techniques, like the Gauss-point-to-segment (GPTS) formulation of Fischer and Wriggers [18] – whose summary is provided here in Appendix A. This feature is advantageous over mortar methods due to the simplicity of GPTS contact formulations. We therefore consider this approach in the present work. Note, however, that while isogeometric contact can remove most artificial discontinuities within the contact zone, physical discontinuities are still present in case of an edge contact involved in simulations. In such case, a segmentation at the edge often becomes necessary in order to provide a proper numerical integration and maintain the robustness. This is discussed e.g. in [1,19].

It is worth mentioning that isogeometric discretization techniques help to improve the robustness of other contact methods as well, e.g. a collocation method [20], or a combination of a mortar method and the isogeometric discretization [7]. A comprehensive overview on the topic of isogeometric contact can be found in e.g. [21].

Apart from the isogeometric discretization, our present work is motivated by a recent advancement in the context of Newton solution techniques with the introduction of the so-called Mixed Interpolation Point method (MIP) [22]. It offers an improvement in the robustness of the Newton method in a displacement-based finite element formulation for structural problems. The improved robustness is indicated by the convergence behavior of Newton iterations given a larger load step size, and hence provides advantage in efficiency over the classical Newton method.

The idea of the MIP method in the original formulation of Magisano et al. [22] is to relax the constitutive equations at integration points, leading to an iterative scheme for computation of tangent stiffness matrices over the Newton iterations. The relaxation here implies that the stress variables are extrapolated at integration points, and hence it is not required to satisfy a given stress–strain relation at every Newton iteration. Instead, the given stress–strain relations are satisfied with convergence of a load step.

Although the MIP method modifies the tangent stiffness matrices, the residual vector resulting from MIP is identical to that in the displacement-based formulation. Consequently, only the convergence behavior of Newton iterations is altered, while the obtained solution is identical to the one from the displacement-based formulation. Further, an implementation of the MIP method is a simple extension from an existing displacement-based finite element code. Yet, the improvement of the robustness is shown to be significant in many cases, e.g. for geometrically non-linear structural problems [22,23], nonlinear planar Kirchhoff rods [24], isogeometric geometrically-non-linearity in solid shells [25], Koiter shells [26], Kirchhoff–Love shells [27], shell coupling [28], large rotational

beam [29,30], dynamic analysis of elastic structures [31], shell buckling [32,33], as well as for beams and shells with material nonlinearity [34].

In this contribution, we present a mixed interpolation point method in the context of frictionless contact formulations. To this end, we start with the perturbed Lagrange multiplier potential of Simo et al. [35] to enforce the contact constraint over the contact surface, where the contact pressure is considered as an additional unknown field apart from the displacement one. As usual, a weak form is obtained from the variational principle. We then discretize the displacement field of the contact surface by smooth isogeometric shape functions. The contact pressure unknown, on the other hand, is solved directly at integration points. A residual vector and its corresponding tangent stiffness matrix are obtained from the discretized weak form and its consistent linearization, respectively. Further, we derive a penalty procedure by eliminating the contact pressure unknown at integration points from the global system of equations. Note that our treatment of the contact pressure here for the MIP method is distinct from Simo et al. [35] for the original perturbed Lagrange multiplier method. There, the contact pressure is considered constant over a contact element. I.e. the contact pressure is interpolated by a constant shape function. As a result, static condensation of the contact pressure unknown can be obtained, but its reduced residual vector as well as the reduced tangent stiffness matrix differ from the standard penalty formulation.

We structure the remaining sections as follows: Section 2 presents a brief geometrical description of the contact surface. The definition of the normal contact gap and its variation and linearization are given in Section 3. The weak form derived from the perturbed Lagrange multiplier potential is provided in Section 4. Then in Section 5, we present the isogeometric discretization of the contact gap and related geometrical quantities. Section 6 provides a detailed derivation of the contact finite element residual and its tangent stiffness matrix, as well as the static condensation of the contact pressure. In Section 7, we assess the accuracy, robustness, and the efficiency of the proposed MIP formulation via several numerical examples. Finally, Section 8 concludes the paper.

## 2. Contact surface description

This section lists essential geometrical objects that we use to describe a contact surface, which is the boundary of a body in consideration.

At any time $t$, a point $\boldsymbol{x}$ in $\mathcal{R}^3$ on the boundary (surface) of body $\mathcal{B}$, denoted by $\gamma = \partial\mathcal{B}$, is defined by the one-to-one mapping from a point $\boldsymbol{\xi} \hat{=} (\xi^1, \xi^2)$ in the 2D-manifold parameter space $\mathcal{P}$ as

$$\boldsymbol{x} = \boldsymbol{x}(\boldsymbol{\xi}, t) \ . \tag{1}$$

The tangent vectors at $\boldsymbol{x} \in \gamma$ can then be defined by

$$\boldsymbol{a}_\alpha := \frac{\partial \boldsymbol{x}}{\partial \xi^\alpha} = \boldsymbol{x}_{,\alpha} \ , \quad (\alpha = 1, 2) \ , \tag{2}$$

and from this, the unit normal vector can be defined as

$$\boldsymbol{n} := \frac{\boldsymbol{a}_1 \times \boldsymbol{a}_2}{\|\boldsymbol{a}_1 \times \boldsymbol{a}_2\|} \ . \tag{3}$$

With respect to the base $\{\boldsymbol{a}_1, \boldsymbol{a}_2, \boldsymbol{n}\}$, one can define the components

$$b_{\alpha\beta} = \boldsymbol{n} \cdot \boldsymbol{a}_{\alpha,\beta} \ , \tag{4}$$

$$a_{\alpha\beta} = \boldsymbol{a}_\alpha \cdot \boldsymbol{a}_\beta \qquad \text{and} \qquad a^{\alpha\beta} = [a_{\alpha\beta}]^{-1} \ , \tag{5}$$

of the curvature and the metric tensor, respectively. The dual tangent vectors $\boldsymbol{a}^\alpha$ relate to the tangent vector (2) by[1]

$$\boldsymbol{a}^\alpha = a^{\alpha\beta}\, \boldsymbol{a}_\beta \ , \tag{6}$$

which satisfies $\boldsymbol{a}^\alpha \cdot \boldsymbol{a}_\beta = \delta^\alpha_\beta$.

## 3. Contact kinematics

In this section, we define the normal contact gap, which is used to describe the impenetrability constraint for contact problems. The variation and linearization is also briefly discussed.

[1] In this paper, the summation convention is applied for repeated Greek indices taking values from 1 to 2.

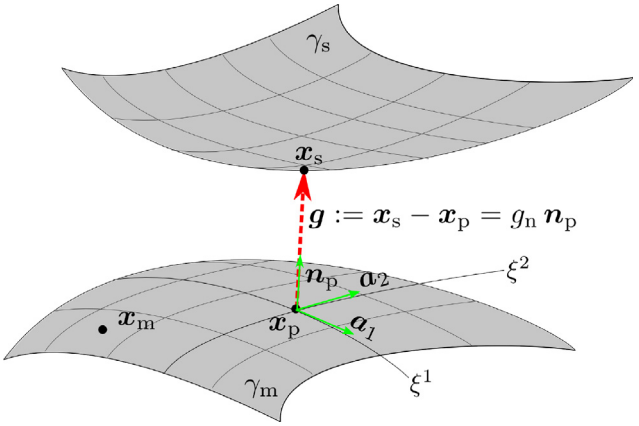


**Fig. 1.** Contact kinematics: definition of the point-wise and signed normal gap $g_n$ between slave surface $\gamma_s$ and the master surface $\gamma_m$ at the current configuration.

Consider a contact problem of two deformable bodies in $\mathcal{R}^3$. In order to formulate the relative interaction between the two contact surfaces of the two bodies at the current configuration, one of the two contact surfaces is assigned as slave and denoted by $\gamma_s$, and the other is assigned as master and denoted by $\gamma_m$. With this, the signed normal gap can be defined by, see Fig. 1.

$$g_n \;\coloneqq\; (\boldsymbol{x}_s - \boldsymbol{x}_p)\cdot \boldsymbol{n}_p \;, \tag{7}$$

where $\boldsymbol{x}_p \in \gamma_m$ denotes the closest projection point from a slave point $\boldsymbol{x}_s \in \gamma_s$ onto the master surface $\gamma_m$, and $\boldsymbol{n}_p$ is the master surface normal at $\boldsymbol{x}_p$. The sign of the normal gap $g_n$ helps in distinction between the cases of penetration ($g_n < 0$) and separation ($g_n > 0$) of the two contact surfaces.

The variation of $g_n$ follows from (7) as

$$\delta g_n = (\delta \boldsymbol{x}_s - \delta \boldsymbol{x}_p)\cdot \boldsymbol{n}_p \;, \tag{8}$$

where we have used the identity $(\boldsymbol{x}_s - \boldsymbol{x}_p)\cdot \delta \boldsymbol{n}_p = g_n\, \boldsymbol{n}_p \cdot \delta \boldsymbol{n}_p = 0$, following from $\boldsymbol{n}_p \cdot \boldsymbol{n}_p = 1$.

Similarly, for linearization of $g_n$, one gets

$$\Delta g_n = (\Delta \boldsymbol{x}_s - \Delta \boldsymbol{x}_p)\cdot \boldsymbol{n}_p \;, \tag{9}$$

where $\Delta$ denotes an increment. Further, linearization of $\delta g_n$ is

$$\Delta\delta g_n \coloneqq \Delta \boldsymbol{n}_p \cdot \left(\delta \boldsymbol{x}_s - \delta \boldsymbol{x}_p\right) - \boldsymbol{n}_p \cdot \delta \boldsymbol{a}_\alpha^p\, \Delta\xi^\alpha \;. \tag{10}$$

## 4. Weak form for the contact constraint

The contact surface $\gamma_s$ generally includes the active contact zone, denoted $\gamma_s^A$, and the inactive contact zone $\gamma_s^I$, that is $\gamma_s = \gamma_s^A \cup \gamma_s^I$. Physically, one observes the contact pressure $\lambda$ vanished in $\gamma_s^I$, and there is no contact gap seen in $\gamma_s^A$. These can mathematically be expressed in the form of the Karush–Kuhn–Tucker conditions as

$$\begin{aligned} &g_n = 0, \quad \text{and} \quad \lambda > 0 \qquad \text{for } \forall\, \boldsymbol{x} \in \gamma_s^A \;, \\ &g_n > 0, \quad \text{and} \quad \lambda = 0 \qquad \text{for } \forall\, \boldsymbol{x} \in \gamma_s^I \;. \end{aligned} \tag{11}$$

These equations can be combined into the equality constraint

$$\lambda\, g_n = 0 \quad \text{for } \forall\, \boldsymbol{x} \in \gamma_s \;. \tag{12}$$

Here, we consider that the zero contact pressure condition within $\gamma_s^I$ is done by an active-set strategy (see Remark 6.4). This effectively requires only the impenetrability constraint $g_n = 0$ within $\gamma_s^A$, which is enforced here by the perturbed Lagrange multiplier potential [35]

$$\Pi_c(\boldsymbol{x}, \lambda) = \int_{\Gamma_s} \lambda\, g_n \,\mathrm{d}S - \frac{1}{2}\int_{\Gamma_s} \frac{1}{\epsilon}\,\lambda^2 \,\mathrm{d}S \;, \tag{13}$$

where $\Gamma_{\rm s}$ is chosen as the slave surface at the reference configuration, $\lambda$ is the Lagrange multiplier and represents the apparent contact pressure, and $\epsilon > 0$ denotes the penalty parameter. Requiring the vanishing of $\delta\Pi_{\rm c}$, the contact virtual work thus reads

$$\delta\Pi_{\rm c}(\boldsymbol{x},\lambda) = \int_{\Gamma_{\rm s}} \lambda\,\delta g_{\rm n}\,{\rm d}S + \int_{\Gamma_{\rm s}} \bar{g}_{\rm n}\,\delta\lambda\,{\rm d}S = 0 \tag{14}$$

where

$$\bar{g}_{\rm n} := g_{\rm n} - \frac{\lambda}{\epsilon} \tag{15}$$

denotes the relaxed contact gap for the variation of contact pressure $\lambda$. Since $\delta g_{\rm n}(\boldsymbol{x})$ and $\delta\lambda$ are considered to be independent variables, the vanishing of $\delta\Pi_{\rm c}$ implies the two integral terms in (14) to be zero. The first term corresponds to the Lagrange multiplier virtual work, which enforces the impenetrability constraint $g_{\rm n} = 0$, while the second term implies the local (point-wise) contact constitution

$$\lambda = \epsilon\, g_{\rm n}. \tag{16}$$

If inserting this contact constitution into the first term of (14) and considering Eq. (8), one in turn gets the penalty (pure displacement-based) contact formulation of Fischer and Wriggers [18] as

$$\delta\Pi_{\rm c}(\boldsymbol{x}) = \int_{\Gamma_{\rm s}} \boldsymbol{T}_{\rm c}\cdot(\delta\boldsymbol{x}_{\rm s} - \delta\boldsymbol{x}_{\rm p})\,{\rm d}S = 0\ , \qquad \text{with} \quad \boldsymbol{T}_{\rm c} := g_{\rm n}\,\boldsymbol{n}_{\rm p}\ . \tag{17}$$

For the sake of convenient comparisons in subsequent sections, Appendix A summarizes the contact finite element forces and contact stiffness matrices resulting from Eq. (17), and we refer to this formulation as the standard penalty (displacement-based) contact formulation, or STD in short.

**Remark 4.1.** In Section 6, we will employ the so-called mixed interpolation point method (MIP) of Magisano et al. [22] in order to relax the contact constitution (16) by providing an extrapolation of contact pressure $\lambda$ at integration points. Note, that this approach is distinct from the treatment of Simo et al. [35]. There, the contact constitution (16) is also relaxed, but it is done by introducing a suitable interpolation of $\lambda$ in a contact element. The treatment of Simo et al. [35] results in a so-called mixed contact formulation.

## 5. Isogeometric discretization of contact surfaces

For smooth slave and master contact surfaces, we consider the isogeometric discretization [4]

$$\begin{aligned}
\boldsymbol{x}_{\rm s} &= \mathbf{N}_e\,\mathbf{x}_e\ ,\\
\delta\boldsymbol{x}_{\rm s} &= \mathbf{N}_e\,\delta\mathbf{x}_e\ ,\\
\delta\boldsymbol{a}^{\rm s}_{\alpha} &= \delta\boldsymbol{x}_{{\rm s},\alpha} = \mathbf{N}_{e,\alpha}\,\delta\mathbf{x}_e\ ,\\
\boldsymbol{x}_{\rm m} &= \mathbf{N}_{\hat{e}}\,\mathbf{x}_{\hat{e}}\ ,\\
\delta\boldsymbol{x}_{\rm m} &= \mathbf{N}_{\hat{e}}\,\delta\mathbf{x}_{\hat{e}}\ ,
\end{aligned} \tag{18}$$

where $\mathbf{N}$ denotes the element shape function array, $\mathbf{x}$ is an array containing position vectors of control points, and the indices $e$ and $\hat{e}$ denote the element index of the slave and master element, respectively.

Applying (18) to Eq. (8) gives the discretized form of $\delta g_{\rm n}$ as

$$\delta g_{\rm n} = \boldsymbol{n}_{\rm p}\cdot\Big[\mathbf{N}_e(\boldsymbol{\xi}^{\rm s})\,\delta\mathbf{x}_e - \mathbf{N}_{\hat{e}}(\boldsymbol{\xi}^{\rm p})\,\delta\mathbf{x}_{\hat{e}}\Big]\ . \tag{19}$$

Similarly for Eq. (9), we have the discretized form of $\Delta g_{\rm n}$ as

$$\Delta g_{\rm n} = \boldsymbol{n}_{\rm p}\cdot\Big[\mathbf{N}_e(\boldsymbol{\xi}^{\rm s})\,\Delta\mathbf{x}_e - \mathbf{N}_{\hat{e}}(\boldsymbol{\xi}^{\rm p})\,\Delta\mathbf{x}_{\hat{e}}\Big]\ . \tag{20}$$

Further, for linearization of $\Delta\delta g_{\rm n}$ from Eq. (10), it should be noted that $\boldsymbol{n}_{\rm p} = \boldsymbol{n}(\boldsymbol{\xi}_{\rm p})$ is a complicated function

$$\boldsymbol{n}_{\rm p} = \boldsymbol{n}_{\rm p}\big(\boldsymbol{x}_{\rm s},\ \boldsymbol{\xi}_{\rm p}(\boldsymbol{x},\mathbf{x}_{\hat{e}}),\ g_{\rm n}(\boldsymbol{x}_{\rm s},\boldsymbol{x}_{\rm p})\big)\ . \tag{21}$$

The linearization of $\boldsymbol{n}_{\rm p}$ can be found, e.g. in [36] as

$$\Delta\boldsymbol{n}_{\rm p} = \frac{\partial\boldsymbol{n}_{\rm p}}{\partial\mathbf{x}_e}\,\Delta\mathbf{x}_e + \frac{\partial\boldsymbol{n}_{\rm p}}{\partial\mathbf{x}_{\hat{e}}}\,\Delta\mathbf{x}_{\hat{e}}\ , \tag{22}$$

where

$$\begin{aligned}\frac{\partial \boldsymbol{n}_{\mathrm{p}}}{\partial \mathbf{x}_e} &= \frac{1}{g_{\mathrm{n}}}\left(\boldsymbol{I}-\boldsymbol{n}_{\mathrm{p}}\otimes\boldsymbol{n}_{\mathrm{p}}-c_{\mathrm{p}}^{\alpha\beta}\,\boldsymbol{a}_{\alpha}^{\mathrm{p}}\otimes\boldsymbol{a}_{\beta}^{\mathrm{p}}\right)\mathbf{N}_e\ ,\\ \frac{\partial \boldsymbol{n}_{\mathrm{p}}}{\partial \mathbf{x}_{\hat{e}}} &= -\frac{1}{g_{\mathrm{n}}}\left(\boldsymbol{I}-\boldsymbol{n}_{\mathrm{p}}\otimes\boldsymbol{n}_{\mathrm{p}}-c_{\mathrm{p}}^{\alpha\beta}\,\boldsymbol{a}_{\alpha}^{\mathrm{p}}\otimes\boldsymbol{a}_{\beta}^{\mathrm{p}}\right)\mathbf{N}_{\hat{e}}-c_{\mathrm{p}}^{\alpha\beta}\,\boldsymbol{a}_{\alpha}^{\mathrm{p}}\otimes\boldsymbol{n}_{\mathrm{p}}\,\mathbf{N}_{\hat{e},\beta}\ ,\end{aligned} \tag{23}$$

with $c_{\mathrm{p}}^{\alpha\beta} := [a_{\alpha\beta}^{\mathrm{p}} - g_{\mathrm{n}}\, b_{\alpha\beta}^{\mathrm{p}}]^{-1}$. Furthermore, one has [36]

$$\Delta\xi^{\alpha} = \frac{\partial \xi^{\alpha}}{\partial \mathbf{x}_e}\,\Delta\mathbf{x}_e + \frac{\partial \xi^{\alpha}}{\partial \mathbf{x}_{\hat{e}}}\,\Delta\mathbf{x}_{\hat{e}}\ , \tag{24}$$

where

$$\begin{aligned}\frac{\partial \xi^{\alpha}}{\partial \mathbf{x}_e} &= c_{\mathrm{p}}^{\alpha\beta}\,\boldsymbol{a}_{\beta}^{\mathrm{p}}\,\mathbf{N}_e\ ,\\ \frac{\partial \xi^{\alpha}}{\partial \mathbf{x}_{\hat{e}}} &= -c_{\mathrm{p}}^{\alpha\beta}\left(\boldsymbol{a}_{\beta}^{\mathrm{p}}\,\mathbf{N}_{\hat{e}}-g_{\mathrm{n}}\,\boldsymbol{n}_{\mathrm{p}}\,\mathbf{N}_{\hat{e},\beta}\right)\ .\end{aligned} \tag{25}$$

Inserting expressions (22) and (24) into Eq. (10) we find

$$\begin{aligned}\Delta\delta g_{\mathrm{n}} &= \delta\mathbf{x}_e\cdot\left(\mathbf{N}_e^{\mathrm{T}}\,\frac{\partial \boldsymbol{n}_{\mathrm{p}}}{\partial \mathbf{x}_e}\,\Delta\mathbf{x}_e+\mathbf{N}_e^{\mathrm{T}}\,\frac{\partial \boldsymbol{n}_{\mathrm{p}}}{\partial \mathbf{x}_{\hat{e}}}\,\Delta\mathbf{x}_{\hat{e}}\right)\\ &- \delta\mathbf{x}_{\hat{e}}\cdot\left(\mathbf{N}_{\hat{e}}^{\mathrm{T}}\,\frac{\partial \boldsymbol{n}_{\mathrm{p}}}{\partial \mathbf{x}_e}+\mathbf{N}_{\hat{e},\alpha}^{\mathrm{T}}\,\boldsymbol{n}_{\mathrm{p}}\otimes\frac{\partial \xi^{\alpha}}{\partial \mathbf{x}_e}\right)\Delta\mathbf{x}_e\\ &- \delta\mathbf{x}_{\hat{e}}\cdot\left(\mathbf{N}_{\hat{e}}^{\mathrm{T}}\,\frac{\partial \boldsymbol{n}_{\mathrm{p}}}{\partial \mathbf{x}_{\hat{e}}}+\mathbf{N}_{\hat{e},\alpha}^{\mathrm{T}}\,\boldsymbol{n}_{\mathrm{p}}\otimes\frac{\partial \xi^{\alpha}}{\partial \mathbf{x}_{\hat{e}}}\right)\Delta\mathbf{x}_{\hat{e}}\ .\end{aligned} \tag{26}$$

## 6. Mixed interpolation point method for contact (MIP)

In this section, we apply the mixed interpolation point method of Magisano et al. [22] to a discretized expression of contact virtual work (14). Accordingly, the residual vector and corresponding stiffness matrix are derived.

### 6.1. Contact residual vector

In order to obtain the residual vector from the contact virtual work (14), one discretizes Eq. (14) in the element-wise manner as

$$\delta\Pi_{\mathrm{c}}(\mathbf{x}_{\mathrm{s}},\mathbf{x}_{\mathrm{m}},\lambda) = \sum_{e=1}^{n_{\mathrm{el}}}\delta\Pi_{\mathrm{c}}^{\mathrm{e}}(\mathbf{x}_e,\mathbf{x}_{\hat{\mathrm{e}}},\lambda) = 0\ , \tag{27}$$

where $\mathbf{x}_{\mathrm{s}}$ and $\mathbf{x}_{\mathrm{m}}$ denote the arrays of position vectors of all slave and master control points, respectively, $n_{\mathrm{el}}$ is the total number of slave elements, and

$$\delta\Pi_{\mathrm{c}}^{\mathrm{e}}(\mathbf{x}_e,\mathbf{x}_{\hat{\mathrm{e}}},\lambda) = \int_{\Gamma_{\mathrm{s}}^e}\lambda\,\delta g_{\mathrm{n}}\,\mathrm{d}S\ +\ \int_{\Gamma_{\mathrm{s}}^e}\bar{g}_{\mathrm{n}}\,\delta\lambda\,\mathrm{d}S\ . \tag{28}$$

Further, we employ the mixed interpolation point method of Magisano et al. [22] over each slave element $e$, which aims to solve the contact equilibrium for unknown $\lambda$ directly at integration points apart from nodal displacement unknowns. That is, inserting Eq. (19) into Eq. (27) and applying a quadrature rule gives

$$\begin{aligned}\delta\Pi_{\mathrm{c}}(\mathbf{x}_{\mathrm{s}},\mathbf{x}_{\mathrm{m}},\lambda) &= \sum_{i=1}^{a}\delta\mathbf{x}_e^i\cdot\mathbf{N}_e^{\mathrm{T}}(\boldsymbol{\xi}_i^{\mathrm{s}})\,\boldsymbol{t}_{\mathrm{c}}^i\,w_i\ -\sum_{i=1}^{a}\delta\mathbf{x}_{\hat{e}}^i\cdot\mathbf{N}_{\hat{e}}^{\mathrm{T}}(\boldsymbol{\xi}_i^{\mathrm{p}})\,\boldsymbol{t}_{\mathrm{c}}^i\,w_i\ +\ \sum_{i=1}^{a}(w_i\,\bar{g}_{\mathrm{n}}^i)\,\delta\lambda_i\\ &= \delta\mathbf{x}_{\mathrm{s}}\cdot\mathbf{r}_{\mathrm{s}}\ +\ \delta\mathbf{x}_{\mathrm{m}}\cdot\mathbf{r}_{\mathrm{m}}+\ \sum_{i=1}^{a}\tilde{g}_{\mathrm{n}}^i\,\delta\lambda_i\ .\end{aligned} \tag{29}$$

Here, $a$ and $i$ denote the total number of (active) integration points and their (global) index over the slave surface $\Gamma_{\mathrm{s}}$, respectively. Arrays $\delta\mathbf{x}_e^i$ and $\delta\mathbf{x}_{\hat{e}}^i$ are variations of control-point positions of slave and master elements associated with integration point $i$, respectively. Vector $\boldsymbol{\xi}_i^{\mathrm{p}} \in \mathcal{P}_{\mathrm{m}}$ denotes the closest projection point from corresponding

integration point $\boldsymbol{\xi}_i^{\mathrm{s}} \in \mathcal{P}_{\mathrm{s}}$. The scalar $w_i \in \Gamma_{\mathrm{s}}$ is the referential area element, related to the parametric area element $\mathrm{d}\square_i := \mathrm{d}\xi_i^1\,\mathrm{d}\xi_i^2 \in \mathcal{P}_{\mathrm{s}}$ as

$$w_i = J_\square\,\mathrm{d}\square_i\ , \qquad \text{with} \quad J_\square := \sqrt{\det[A_{\alpha\beta}]}\ , \tag{30}$$

where $A_{\alpha\beta}$ are metric components of the slave surface at the reference configuration, and $J_\square$ is the area stretch from $\mathcal{P}_{\mathrm{s}}$ to $\Gamma_{\mathrm{s}}^e$.[2]

Further in Eq. (29), we have defined the weighted-relaxed gaps at integration point $i$

$$\tilde{g}_{\mathrm{n}}^i \quad := \quad w_i\,\bar{g}_{\mathrm{n}}^i\ , \tag{31}$$

and the contact residual vectors on slave and master control points as

$$\mathbf{r}_{\mathrm{s}} \quad := \quad \sum_{i=1}^{a} \mathop{\mathrm{A}}_{e} \mathbf{N}_e^{\mathrm{T}}(\boldsymbol{\xi}_i^{\mathrm{s}})\,\boldsymbol{t}_{\mathrm{c}}^i\,w_i\ , \quad \mathbf{r}_{\mathrm{m}} := -\sum_{i=1}^{a} \mathop{\mathrm{A}}_{\hat{e}} \mathbf{N}_{\hat{e}}^{\mathrm{T}}(\boldsymbol{\xi}_i^{\mathrm{p}})\,\boldsymbol{t}_{\mathrm{c}}^i\,w_i\ , \quad \text{with} \qquad \boldsymbol{t}_{\mathrm{c}}^i := \lambda_i\,\boldsymbol{n}_{\mathrm{p}}\ , \tag{32}$$

where $\boldsymbol{t}_{\mathrm{c}}^i$ is the apparent contact traction at integration point $i$, and $\mathrm{A}$ denotes the assembly operator.

Furthermore, in view of Eq. (29), we can define the so-called global generalized vector of unknowns as

$$\mathbf{u} := \left[\mathbf{x}_{\mathrm{s}}^{\mathrm{T}}\ ,\quad \mathbf{x}_{\mathrm{m}}^{\mathrm{T}}\ ,\quad \lambda_1\ ,\quad \lambda_2\ ,\quad .\ .\ .\ ,\quad \lambda_a\right]^{\mathrm{T}}\ . \tag{33}$$

With this, Eq. (27) can be expressed as

$$\delta\Pi_{\mathrm{c}}(\mathbf{u}) = \delta\mathbf{u}\cdot\mathbf{r}_{\mathrm{c}}(\mathbf{u}) = 0\ , \qquad \text{for} \quad \forall\delta\mathbf{u} \in \mathcal{V}^h\ , \tag{34}$$

where $\mathcal{V}^h$ denotes the set of kinematically admissible variations for the control points and pressure at integration points, and

$$\mathbf{r}_{\mathrm{c}}(\mathbf{u}) = \left[\mathbf{r}_{\mathrm{s}}^{\mathrm{T}}\ ,\quad \mathbf{r}_{\mathrm{m}}^{\mathrm{T}}\ ,\quad \tilde{g}_{\mathrm{n}}^1\ ,\quad \tilde{g}_{\mathrm{n}}^2\ ,\quad .\ .\ .\ ,\quad \tilde{g}_{\mathrm{n}}^a\right]^{\mathrm{T}} \tag{35}$$

is the global contact residual vector.

**Remark 6.1.** It should be noted in Eq. (29), that no interpolation of the contact pressure $\lambda$ has been made from integration point to integration point. This corresponds to an application of the Dirac delta function to the fields $\lambda$ and $\delta\lambda$ from the continuum equation (28), which somewhat resembles the point collocation method and allows for an elimination of contact pressure unknowns (i.e. a static condensation) from the global system of equation, see Section 6.2.2. This is, however, different from the pure collocation scheme, where the contact pressure is collocated in order to directly enforce the contact impenetrability condition $g_{\mathrm{n}} = 0$. Instead, the collocation here is to enforce only the constitutive equation (16) (or equivalently $\bar{g}_{\mathrm{n}} = 0$) discretely at integration points for the second term of Eq. (28).

**Remark 6.2.** Instead of the element-wise integration as is used here, a patch-wise integration can also be used for the contact virtual work (27). In such case, the element index $e$ in our presented formulation here and henceforth is simply replaced by a patch index, and the element shape function array $\mathbf{N}$ is replaced by the B-Spline shape functions of the patch.

### 6.2. Contact stiffness matrices

In this section, we derive the contact stiffness matrices following from the MIP-discretized virtual work (29) for the Newton–Raphson method. Note, that the contact pressure $\lambda_i$ at integration points is unknown and thus contributes to additional degrees of freedom in the global system of equations. The tangent matrix resulting from this is referred to as the full contact stiffness matrices. We then perform a static condensation of the stiffness matrix by elimination of the unknowns $\lambda_i$ at integration points.

[2] Note that for the Gaussian quadrature rule and the parametric domain $\mathcal{P}$ being the square of area 4, the parametric element area $\mathrm{d}\square_i$ is identical to the Gauss-point weight.

### 6.2.1. Full contact stiffness matrices

To obtain the contact stiffness matrices, we start with the linearization of $\delta\Pi_{\mathrm{c}}$ in Eq. (27) as

$$\Delta\delta\Pi_{\mathrm{c}} = \int_{\Gamma_{\mathrm{s}}} \Delta\delta g_{\mathrm{n}}\,\lambda\,\mathrm{d}S + \int_{\Gamma_{\mathrm{s}}} \delta g_{\mathrm{n}}\,\Delta\lambda\,\mathrm{d}S + \int_{\Gamma_{\mathrm{s}}} \delta\lambda\,\Delta g_{\mathrm{n}}\,\mathrm{d}S - \int_{\Gamma_{\mathrm{s}}} \frac{1}{\epsilon}\,\delta\lambda\,\Delta\lambda\,\mathrm{d}S\,. \tag{36}$$

Inserting approximations (19), (20), (26), and the mixed interpolation for the pressure field $\lambda$ with the same quadrature rule used in Eq. (29) into Eq. (36), we find

$$\begin{aligned}\Delta\delta\Pi_{\mathrm{c}} = &\sum_i^a \delta\mathbf{x}_e^i \cdot \mathbf{k}_{ee}^{ii}\,\Delta\mathbf{x}_e^i + \sum_i^a \delta\mathbf{x}_e^i \cdot \mathbf{k}_{e\hat{e}}^{ii}\,\Delta\mathbf{x}_{\hat{e}}^i + \sum_i^a \delta\mathbf{x}_e^i \cdot \mathbf{k}_{e\mathrm{g}}^{ii}\,\Delta\lambda_i \\ &+ \sum_i^a \delta\mathbf{x}_{\hat{e}}^i \cdot \mathbf{k}_{\hat{e}e}^{ii}\,\Delta\mathbf{x}_e^i + \sum_i^a \delta\mathbf{x}_{\hat{e}}^i \cdot \mathbf{k}_{\hat{e}\hat{e}}^{ii}\,\Delta\mathbf{x}_{\hat{e}}^i + \sum_i^a \delta\mathbf{x}_{\hat{e}}^i \cdot \mathbf{k}_{\hat{e}\mathrm{g}}^{ii}\,\Delta\lambda_i \\ &+ \sum_i^a \delta\lambda_i \cdot \mathbf{k}_{\mathrm{g}e}^{ii}\,\Delta\mathbf{x}_e^i + \sum_i^a \delta\lambda_i \cdot \mathbf{k}_{\mathrm{g}\hat{e}}^{ii}\,\Delta\mathbf{x}_{\hat{e}}^i + \sum_i^a \delta\lambda_i \cdot k_{\mathrm{gg}}^{ii}\,\Delta\lambda_i\,,\end{aligned} \tag{37}$$

where we have defined the elemental stiffness matrix at integration point $i$ as

$$\begin{aligned}\mathbf{k}_{ee}^{ii} &:= \mathbf{M}^{ee}\,w_i\,\lambda_i\,, & \mathbf{k}_{e\hat{e}}^{ii} &:= \mathbf{M}^{e\hat{e}}\,w_i\,\lambda_i\,,\\ \mathbf{k}_{\hat{e}e}^{ii} &:= -\mathbf{M}^{\hat{e}e}\,w_i\,\lambda_i\,, & \mathbf{k}_{\hat{e}\hat{e}}^{ii} &:= -\mathbf{M}^{\hat{e}\hat{e}}\,w_i\,\lambda_i\,,\\ \mathbf{k}_{e\mathrm{g}}^{ii} &:= \mathbf{G}_e\,w_i\,, & \mathbf{k}_{\mathrm{g}e}^{ii} &:= (\mathbf{k}_{e\mathrm{g}}^{ii})^{\mathrm{T}}\,,\\ \mathbf{k}_{\hat{e}\mathrm{g}}^{ii} &:= -\mathbf{G}_{\hat{e}}\,w_i\,, & \mathbf{k}_{\mathrm{g}\hat{e}}^{ii} &:= (\mathbf{k}_{\hat{e}\mathrm{g}}^{ii})^{\mathrm{T}}\,,\\ k_{\mathrm{gg}}^{ii} &:= -\frac{1}{\epsilon}\,w_i\,,\end{aligned} \tag{38}$$

with

$$\begin{aligned}\mathbf{M}^{ee} &:= \mathbf{N}_e^{\mathrm{T}}\frac{\partial\boldsymbol{n}_{\mathrm{p}}}{\partial\mathbf{x}_e}\,,\\ \mathbf{M}^{e\hat{e}} &:= \mathbf{N}_e^{\mathrm{T}}\frac{\partial\boldsymbol{n}_{\mathrm{p}}}{\partial\mathbf{x}_{\hat{e}}}\,,\\ \mathbf{M}^{\hat{e}e} &:= \mathbf{N}_{\hat{e}}^{\mathrm{T}}\frac{\partial\boldsymbol{n}_{\mathrm{p}}}{\partial\mathbf{x}_e} + \mathbf{N}_{\hat{e},\alpha}^{\mathrm{T}}\,\boldsymbol{n}_{\mathrm{p}}\otimes\frac{\partial\xi^\alpha}{\partial\mathbf{x}_e}\,,\\ \mathbf{M}^{\hat{e}\hat{e}} &:= \mathbf{N}_{\hat{e}}^{\mathrm{T}}\frac{\partial\boldsymbol{n}_{\mathrm{p}}}{\partial\mathbf{x}_{\hat{e}}} + \mathbf{N}_{\hat{e},\alpha}^{\mathrm{T}}\,\boldsymbol{n}_{\mathrm{p}}\otimes\frac{\partial\xi^\alpha}{\partial\mathbf{x}_{\hat{e}}}\,,\\ \mathbf{G}_e &:= \mathbf{N}_e^{\mathrm{T}}(\boldsymbol{\xi}^{\mathrm{s}})\,\boldsymbol{n}_{\mathrm{p}}\,,\\ \mathbf{G}_{\hat{e}} &:= \mathbf{N}_{\hat{e}}^{\mathrm{T}}(\boldsymbol{\xi}^{\mathrm{p}})\,\boldsymbol{n}_{\mathrm{p}}\,.\end{aligned} \tag{39}$$

To obtain a global stiffness matrix compatible with unknown list (33), rewriting Eq. (37) gives

$$\begin{aligned}\Delta\delta\Pi_{\mathrm{c}} = &\ \delta\mathbf{x}_{\mathrm{s}} \cdot \mathbf{k}_{\mathrm{ss}}\,\Delta\mathbf{x}_{\mathrm{s}} + \delta\mathbf{x}_{\mathrm{s}} \cdot \mathbf{k}_{\mathrm{sm}}\,\Delta\mathbf{x}_{\mathrm{m}} + \delta\mathbf{x}_{\mathrm{s}} \cdot \sum_i^a \mathbf{k}_{\mathrm{sg}}^{\cdot i}\,\Delta\lambda_i \\ &+ \delta\mathbf{x}_{\mathrm{m}} \cdot \mathbf{k}_{\mathrm{ms}}\,\Delta\mathbf{x}_{\mathrm{s}} + \delta\mathbf{x}_{\mathrm{m}} \cdot \mathbf{k}_{\mathrm{mm}}\,\Delta\mathbf{x}_{\mathrm{m}} + \delta\mathbf{x}_{\mathrm{m}} \cdot \sum_i^a \mathbf{k}_{\mathrm{mg}}^{\cdot i}\,\Delta\lambda_i \\ &+ \Big(\sum_i^a \delta\lambda_i \cdot \mathbf{k}_{\mathrm{gs}}^{i\cdot}\Big)\,\Delta\mathbf{x}_{\mathrm{s}} + \Big(\sum_i^a \delta\lambda_i \cdot \mathbf{k}_{\mathrm{gm}}^{i\cdot}\Big)\,\Delta\mathbf{x}_{\mathrm{m}} + \sum_i^a \delta\lambda_i \cdot k_{\mathrm{gg}}^{ii}\,\Delta\lambda_i\,,\end{aligned} \tag{40}$$

where we have grouped (assembled) the contribution of all control points on the slave and master surfaces. With these, we have defined

$$\mathbf{k}_{\mathrm{ss}} = \sum_{i=1}^{a} \mathop{\mathbf{A}}_{e} \mathop{\mathbf{A}}_{e} \mathbf{k}_{ee}^{ii} \ , \quad \mathbf{k}_{\mathrm{sm}} = \sum_{i=1}^{a} \mathop{\mathbf{A}}_{e} \mathop{\mathbf{A}}_{\hat{e}} \mathbf{k}_{e\hat{e}}^{ii} \ , \quad \mathbf{k}_{\mathrm{ms}} = \sum_{i=1}^{a} \mathop{\mathbf{A}}_{\hat{e}} \mathop{\mathbf{A}}_{e} \mathbf{k}_{\hat{e}e}^{ii} \ , \quad \mathbf{k}_{\mathrm{mm}} = \sum_{i=1}^{a} \mathop{\mathbf{A}}_{\hat{e}} \mathop{\mathbf{A}}_{\hat{e}} \mathbf{k}_{\hat{e}\hat{e}}^{ii}$$
$$\mathbf{k}_{\mathrm{sg}}^{k.} = \sum_{i=1}^{a} \mathop{\mathbf{A}}_{e} \mathbf{k}_{eg}^{ik} \ , \qquad \mathbf{k}_{\mathrm{gs}}^{k.} = \sum_{i=1}^{a} \mathop{\mathbf{A}}_{e} \mathbf{k}_{ge}^{ki} \ , \qquad \mathbf{k}_{\mathrm{mg}}^{k.} = \sum_{i=1}^{a} \mathop{\mathbf{A}}_{\hat{e}} \mathbf{k}_{\hat{e}g}^{ik} \ , \qquad \mathbf{k}_{\mathrm{gm}}^{k.} = \sum_{i=1}^{a} \mathop{\mathbf{A}}_{\hat{e}} \mathbf{k}_{g\hat{e}}^{ki} \ . \tag{41}$$

Eq. (40) can be expressed in the matrix form

$$\Delta\delta\Pi_{\mathrm{c}} = \underbrace{\begin{bmatrix} \delta\mathbf{x}_{\mathrm{s}} \\ \delta\mathbf{x}_{\mathrm{m}} \\ \delta\lambda_1 \\ \delta\lambda_2 \\ . \\ . \\ . \\ \delta\lambda_a \end{bmatrix}^{\mathrm{T}}}_{\delta\mathbf{u}} \underbrace{\begin{bmatrix} \mathbf{k}_{\mathrm{ss}} & \mathbf{k}_{\mathrm{sm}} & \mathbf{k}_{\mathrm{sg}}^{1} & \mathbf{k}_{\mathrm{sg}}^{2} & \dots & \mathbf{k}_{\mathrm{sg}}^{a} \\ \mathbf{k}_{\mathrm{ms}} & \mathbf{k}_{\mathrm{mm}} & \mathbf{k}_{\mathrm{mg}}^{1} & \mathbf{k}_{\mathrm{mg}}^{2} & \dots & \mathbf{k}_{\mathrm{mg}}^{a} \\ \mathbf{k}_{\mathrm{gs}}^{1} & \mathbf{k}_{\mathrm{gm}}^{1} & k_{\mathrm{gg}}^{11} & k_{\mathrm{gg}}^{12} & \dots & k_{\mathrm{gg}}^{1a} \\ \mathbf{k}_{\mathrm{gs}}^{2} & \mathbf{k}_{\mathrm{gm}}^{2} & k_{\mathrm{gg}}^{21} & k_{\mathrm{gg}}^{22} & \dots & k_{\mathrm{gg}}^{2a} \\ . & . & . & . & & . \\ . & . & . & . & & . \\ . & . & . & . & & . \\ \mathbf{k}_{\mathrm{gs}}^{a} & \mathbf{k}_{\mathrm{gm}}^{a} & k_{\mathrm{gg}}^{a1} & k_{\mathrm{gg}}^{a2} & \dots & k_{\mathrm{gg}}^{aa} \end{bmatrix}}_{=:\mathbf{K}_{\mathrm{c}}} \underbrace{\begin{bmatrix} \Delta\mathbf{x}_{\mathrm{s}} \\ \Delta\mathbf{x}_{\mathrm{m}} \\ \Delta\lambda_1 \\ \Delta\lambda_2 \\ . \\ . \\ . \\ \Delta\lambda_a \end{bmatrix}}_{\Delta\mathbf{u}} \tag{42}$$

where we have defined the global contact stiffness matrix $\mathbf{K}_{\mathrm{c}}$.[3]

On the other hand, to solve Eq. (34) by the Newton–Raphson method, applying Taylor series to Eq. (34) and taking Eq. (42) into account, gives

$$\begin{aligned} \delta\Pi_{\mathrm{c}}(\mathbf{u}+\Delta\mathbf{u}) &= \delta\Pi_{\mathrm{c}}(\mathbf{u}) + \Delta\delta\Pi_{\mathrm{c}} \qquad \approx 0 \\ &= \delta\mathbf{u}\cdot\mathbf{r}_{\mathrm{c}} + \delta\mathbf{u}\cdot\mathbf{K}_{\mathrm{c}}\,\Delta\mathbf{u} \approx 0 \qquad \text{for} \quad \forall\delta\mathbf{u}\in\mathcal{V}^{h} \ . \end{aligned} \tag{43}$$

Since $\delta\mathbf{u}$ is arbitrary, the last equation yields the system of equation

$$\mathbf{K}_{\mathrm{c}}\,\Delta\mathbf{u} = -\mathbf{r}_{\mathrm{c}} \ , \tag{44}$$

whose matrix form reads

$$\begin{bmatrix} \mathbf{k}_{\mathrm{ss}} & \mathbf{k}_{\mathrm{sm}} & \mathbf{k}_{\mathrm{sg}}^{1} & \mathbf{k}_{\mathrm{sg}}^{2} & \dots & \mathbf{k}_{\mathrm{sg}}^{a} \\ \mathbf{k}_{\mathrm{ms}} & \mathbf{k}_{\mathrm{mm}} & \mathbf{k}_{\mathrm{mg}}^{1} & \mathbf{k}_{\mathrm{mg}}^{2} & \dots & \mathbf{k}_{\mathrm{mg}}^{a} \\ \mathbf{k}_{\mathrm{gs}}^{1} & \mathbf{k}_{\mathrm{gm}}^{1} & k_{\mathrm{gg}}^{11} & k_{\mathrm{gg}}^{12} & \dots & k_{\mathrm{gg}}^{1a} \\ \mathbf{k}_{\mathrm{gs}}^{2} & \mathbf{k}_{\mathrm{gm}}^{2} & k_{\mathrm{gg}}^{21} & k_{\mathrm{gg}}^{22} & \dots & k_{\mathrm{gg}}^{2a} \\ . & . & . & . & & . \\ . & . & . & . & & . \\ . & . & . & . & & . \\ \mathbf{k}_{\mathrm{gs}}^{a} & \mathbf{k}_{\mathrm{gm}}^{a} & k_{\mathrm{gg}}^{a1} & k_{\mathrm{gg}}^{a2} & \dots & k_{\mathrm{gg}}^{aa} \end{bmatrix} \begin{bmatrix} \Delta\mathbf{x}_{\mathrm{s}} \\ \Delta\mathbf{x}_{\mathrm{m}} \\ \Delta\lambda_1 \\ \Delta\lambda_2 \\ . \\ . \\ . \\ \Delta\lambda_a \end{bmatrix} = - \begin{bmatrix} \mathbf{r}_{\mathrm{s}} \\ \mathbf{r}_{\mathrm{m}} \\ \tilde{g}_{\mathrm{n}}^{1} \\ \tilde{g}_{\mathrm{n}}^{2} \\ . \\ . \\ . \\ \tilde{g}_{\mathrm{n}}^{a} \end{bmatrix} \tag{45}$$

where the increments $\Delta\mathbf{x}_{\mathrm{s}}$, $\Delta\mathbf{x}_{\mathrm{m}}$, and $\Delta\lambda_i$ are unknown to be solved for at the global level.

[3] In Eq. (42), the scalars with light gray color imply zeros, while the arrays colored in green, blue, and red imply that their matrix multiplication (or dot product) is associated with degrees of freedom at slave control points, master control points, and integration points, respectively.

*6.2.2. Condensed residual vector and stiffness matrices*

Since unknowns $\Delta\lambda_i$ are only associated with integration points, a static condensation is possible. To this end, using Eq. (38), (41), and (31) eliminates $\Delta\lambda_i$ from (45) as

$$\begin{aligned} \Delta\lambda_i &= -\frac{1}{k^{ii}_{gg}} \left( \mathbf{k}^i_{\mathrm{gs}} \cdot \Delta\mathbf{x}_{\mathrm{s}} + \mathbf{k}^i_{\mathrm{gm}} \cdot \Delta\mathbf{x}_{\mathrm{m}} + \tilde{g}^i_{\mathrm{n}} \right) \\ &= \epsilon \left( \mathbf{G}_e \cdot \Delta\mathbf{x}^i_e - \mathbf{G}_{\hat{e}} \cdot \Delta\mathbf{x}^i_{\hat{e}} + \bar{g}^i_{\mathrm{n}} \right) . \end{aligned} \tag{46}$$

The second expression in Eq. (46) follows from inserting Eq. (41) with (38), and considering that only the elements $e$ and $\hat{e}$ that are associated with integration point $i$ are assembled for $\mathbf{k}^i_{\mathrm{gs}}$ and $\mathbf{k}^i_{\mathrm{gm}}$, respectively. Note, that $\Delta\mathbf{x}^i_e$ and $\Delta\mathbf{x}^i_{\hat{e}}$ are global (assembled) quantities. With (46), rearranging Eq. (45) gives the (global) reduced system of equation to be solved for only displacement DOFs as

$$\underbrace{\begin{bmatrix} \bar{\mathbf{k}}_{\mathrm{ss}} & \bar{\mathbf{k}}_{\mathrm{sm}} \\ \bar{\mathbf{k}}_{\mathrm{ms}} & \bar{\mathbf{k}}_{\mathrm{mm}} \end{bmatrix}}_{\bar{\mathbf{K}}_{\mathrm{c}}} \underbrace{\begin{bmatrix} \Delta\mathbf{x}_{\mathrm{s}} \\ \Delta\mathbf{x}_{\mathrm{m}} \end{bmatrix}}_{\Delta\bar{\mathbf{u}}} = - \underbrace{\begin{bmatrix} \bar{\mathbf{r}}_{\mathrm{s}} \\ \bar{\mathbf{r}}_{\mathrm{m}} \end{bmatrix}}_{\bar{\mathbf{f}}_{\mathrm{c}}} , \tag{47}$$

where

$$\begin{aligned} \bar{\mathbf{k}}_{\mathrm{ss}} &= \sum_{i=1}^{a} \mathop{\mathbf{A}}_{e} \mathop{\mathbf{A}}_{e} \left( \mathbf{M}^{ee}\, w_i\, \lambda_i + \epsilon\, \mathbf{G}^{\mathrm{T}}_e\, w_i\, \mathbf{G}_e \right) , \\ \bar{\mathbf{k}}_{\mathrm{sm}} &= \sum_{i=1}^{a} \mathop{\mathbf{A}}_{e} \mathop{\mathbf{A}}_{\hat{e}} \left( \mathbf{M}^{e\hat{e}}\, w_i\, \lambda_i - \epsilon\, \mathbf{G}^{\mathrm{T}}_e\, w_i\, \mathbf{G}_{\hat{e}} \right) , \\ \bar{\mathbf{k}}_{\mathrm{ms}} &= -\sum_{i=1}^{a} \mathop{\mathbf{A}}_{\hat{e}} \mathop{\mathbf{A}}_{e} \left( \mathbf{M}^{\hat{e}e}\, w_i\, \lambda_i + \epsilon\, \mathbf{G}^{\mathrm{T}}_{\hat{e}}\, w_i\, \mathbf{G}_e \right) , \\ \bar{\mathbf{k}}_{\mathrm{mm}} &= -\sum_{i=1}^{a} \mathop{\mathbf{A}}_{\hat{e}} \mathop{\mathbf{A}}_{\hat{e}} \left( \mathbf{M}^{\hat{e}\hat{e}}\, w_i\, \lambda_i + \epsilon\, \mathbf{G}^{\mathrm{T}}_{\hat{e}}\, w_i\, \mathbf{G}_{\hat{e}} \right) \end{aligned} \tag{48}$$

are the contact stiffness matrices evaluated at the integration point level. Further, the residual is reduced to

$$\bar{\mathbf{r}}_{\mathrm{s}} \coloneqq \sum_{i=1}^{a} \mathop{\mathbf{A}}_{e} \mathbf{N}^{\mathrm{T}}_e\, \bar{\boldsymbol{t}}_{\mathrm{c}}\, w_i \ , \quad \bar{\mathbf{r}}_{\mathrm{m}} \coloneqq -\sum_{i=1}^{a} \mathop{\mathbf{A}}_{\hat{e}} \mathbf{N}^{\mathrm{T}}_{\hat{e}}\, \bar{\boldsymbol{t}}_{\mathrm{c}}\, w_i \ , \quad \text{with} \quad \bar{\boldsymbol{t}}_{\mathrm{c}} \coloneqq \epsilon\, g_{\mathrm{n}}\, \boldsymbol{n}_{\mathrm{p}} \ . \tag{49}$$

**Remark 6.3.** In comparison with the standard penalty formulation (STD) of Fischer and Wriggers [18] – see also Appendix A – the reduced residual resulting from the proposed MIP method is identical to that of the STD formulation as the Eqs. (49) and (54) show. However, the stiffness matrices (48) resulting from MIP are now computed based on the extrapolation of the contact pressure $\lambda_i$ from Eq. (46). Meanwhile, the STD stiffness matrices are computed with the requirement $\lambda_i = \epsilon\, g_{\mathrm{n}}$ for every iteration. This is seen from Eq. (56).

**Remark 6.4.** Although we start with the perturbed Lagrange multiplier potential (13), from Eq. (49) we conclude that the MIP contact formulation is eventually a pure displacement-based (penalty type) formulation and it allows for a small violation of the impenetrability constraint. This is useful in the application of the simple active-set strategy, that is purely based on the sign of the contact gap, in order to determine the interface between the active contact zone $\gamma^A_{\mathrm{s}}$ and the inactive contact zone $\gamma^I_{\mathrm{s}}$. Note that a convergence of this active-set strategy is not guaranteed, since no linearization is extracted from its non-linearity. However we observe for the smooth contact surface as adopted here, that a convergence is usually obtained within few iterations, without any further adhoc treatment (like freezing the active-set). See e.g. Fig. 8 in the example 7.3 below.

*6.3. MIP contact algorithm*

As mentioned in Remark 6.3 in Section 6.2.2, since the MIP residual vector is identical to the standard (displacement-based) penalty contact formulation, the implementation is a simple modification of the existing code

**Table 1**
A finite element contact algorithm for the proposed MIP formulation. Here, items marked with blue color imply additional tasks w.r.t. the standard penalty (displacement-based) contact formulation.

1. Loading loop:
- apply load increment or time step
- provide initial guess for the nodal displacements or the current configuration.

2. Contact active-set loop:
- provide initial guess for the contact active-set: e.g. from previous load step.
- provide initial guess for the contact pressure $\lambda_i$ at contact quadrature points $i$.

3. Global Newton–Raphson loop:

4. Loop over the bulk elements:
- loop over quadrature points: compute internal FE forces & tangent matrices.
- assemble the FE forces & tangent matrices into the global matrices.

5. Loop over the slave contact elements $e = 1 \ldots n_{\text{el}}$:

6. Loop over the contact quadrature point $\boldsymbol{\xi}_i^{\text{s}}$ over an element:
- determine current position $\boldsymbol{x}_{\text{s}} \in \gamma_{\text{s}}$ of the quadrature point.
- from $\boldsymbol{x}_{\text{s}}$, find the closest projection point $\boldsymbol{x}_{\text{p}}(\boldsymbol{\xi}_{\text{p}}^i)$ in master element $\hat{e}$.
- evaluate normal gap $g_{\text{n}}$ (Eq. (7)) and geometrical quantities in Section 2
- evaluate the contact active-set.
- If contact quadrature point $i$ is active, then:
  - extrapolate contact pressure $\lambda_i \leftarrow \lambda_i + \Delta\lambda_i$, see Eq. (46).
  - compute contact FE forces and stiffness from Eqs. (49) and (48).
    - assemble contact FE forces ((49)b) & stiffness ((48)b-d) for master elements into global matrices $\bar{\mathbf{f}}_{\text{c}}$ and $\bar{\mathbf{K}}_{\text{c}}$, respectively.
  - store arrays $\mathbf{G}_e$, $\mathbf{G}_{\hat{e}}$, and $\bar{g}_{\text{n}}^i$ – from Eq. (39)(e-f) and Eq. (15), respectively.
- assemble contact FE forces ((49)a) & stiffness ((48)a) for slave elements into global matrices $\bar{\mathbf{f}}_{\text{c}}$ and $\bar{\mathbf{K}}_{\text{c}}$, respectively.

- apply boundary conditions.
- solve the global linear system of equations for the increment $\Delta\mathbf{x}$ of nodal positions.
- update nodal displacements, current configuration, and evaluate error norm.
- compute the pressure increment $\Delta\lambda_i$ at contact quadrature points from Eq. (46)
- check for the convergence of the global Newton–Raphson loop.

- repeat the global Newton–Raphson loop #3 if the contact active-set has changed.

for the computation of the stiffness matrix. Table 1 provides an algorithm for the MIP contact formulation presented above.

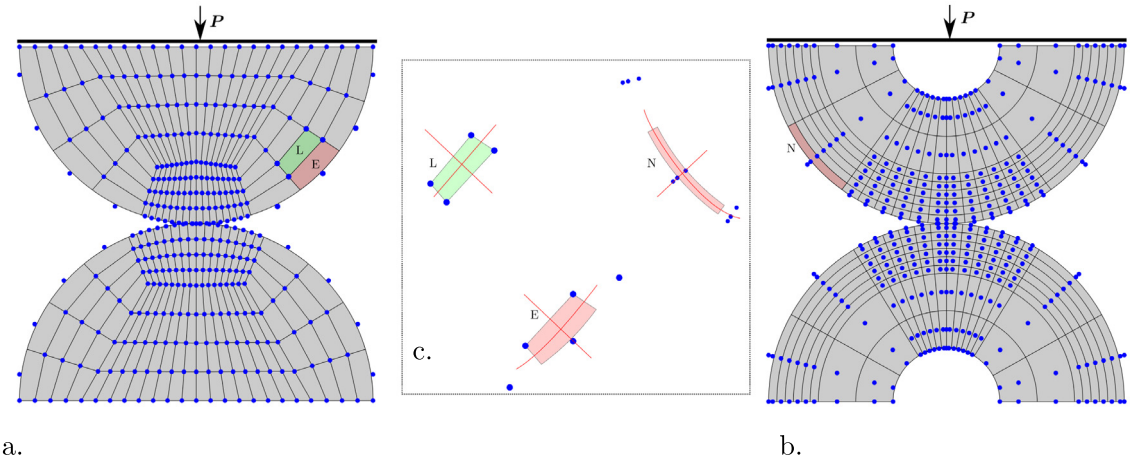


**Fig. 2.** Hertz contact: initial mesh using (a.) NURBS-enriched finite elements (Q1N2) of Corbett and Sauer [16], and (b.) IGA with a single quadratic NURBS patch per body. The Q1N2 mesh consists of linear Lagrangian elements (L) for the bulk and transition elements (E) on the smooth boundary. The extraction of exemplar elements together with their nodes/control points are depicted in (c.). The symmetry in the $x$-direction is exploited in simulations, i.e. only half of the geometry is modeled and all nodes/control points along the symmetry line $X = 0$ are fixed in the $x$-direction.

## 7. Numerical examples

In this section, several numerical examples are presented to demonstrate the accuracy, the robustness and the efficiency of the proposed MIP contact in comparison with the standard (STD) displacement-based contact formulation. Both 2D and 3D contact problems are considered.

For the unit normalization in the examples, we choose a reference length $L_0$, and a reference stress $E_0$ with the unit [force/length$^2$]. Based on these, the unit of reaction forces and penalty parameter are thus $E_0\,L_0^2$ and $E_0/L_0$, respectively.

### *7.1. Hertz contact problem*

The first example is the well-known Hertz's contact problem. We consider the contact between two half of cylinders of the same radius $R = 8\,L_0$, see Fig. 2. The plane strain Neo-Hookean model (see e.g. [37]) is used with $E = 200\,E_0$ and $\nu = 0.3$. With the lower cylinder fixed at its lower edge, the upper cylinder is pressed down by the application of a distributed load with resultant force $P$ on the upper edge.

We consider two types of smooth discretization schemes for contact surfaces, including the NURBS-enriched finite elements (Q1N2) of Corbett and Sauer [16] and quadratic IGA elements as seen in Fig. 2a and b, respectively. Both meshes provide a smooth surface of the cylinders, but in the former mesh linear Lagrange elements (L) are used for the interior bulk.

In particular to the IGA mesh in Fig. 2b, we employ a modified half-cylinder with the hole of radius $0.3\,L_0$. To keep the contact response at the contact interface unaffected by this modification, we constrain all control points on the upper edges, such that they have the same position $y$ in the solution. This is done here by the coupling technique of del Toro Llorens and Kiendl [38], where a control point is assigned as master and all other control points as slave, which follow motion of the master control point in the $y$-direction. The desired external force is then applied on the master control point.

For the subsequent computations, a penalty parameter $\epsilon = 2 \times 10^4\,E_0/L_0$ is used, and we consider either a small load case ($P = 2.5\,E_0\,L_0^2$) or a large load case (with $P = 10\,E_0\,L_0^2$).

Fig. 3a–b. plot the deformed configuration for the large load case. As can be seen, the stress distribution around contact zone with the two meshes is almost identical, regardless of the mesh differences in the far field. A zoom into the contact area is provided in Fig. 3c–d, which shows that the contact constraint is enforced to a high accuracy with the considered penalty parameter.

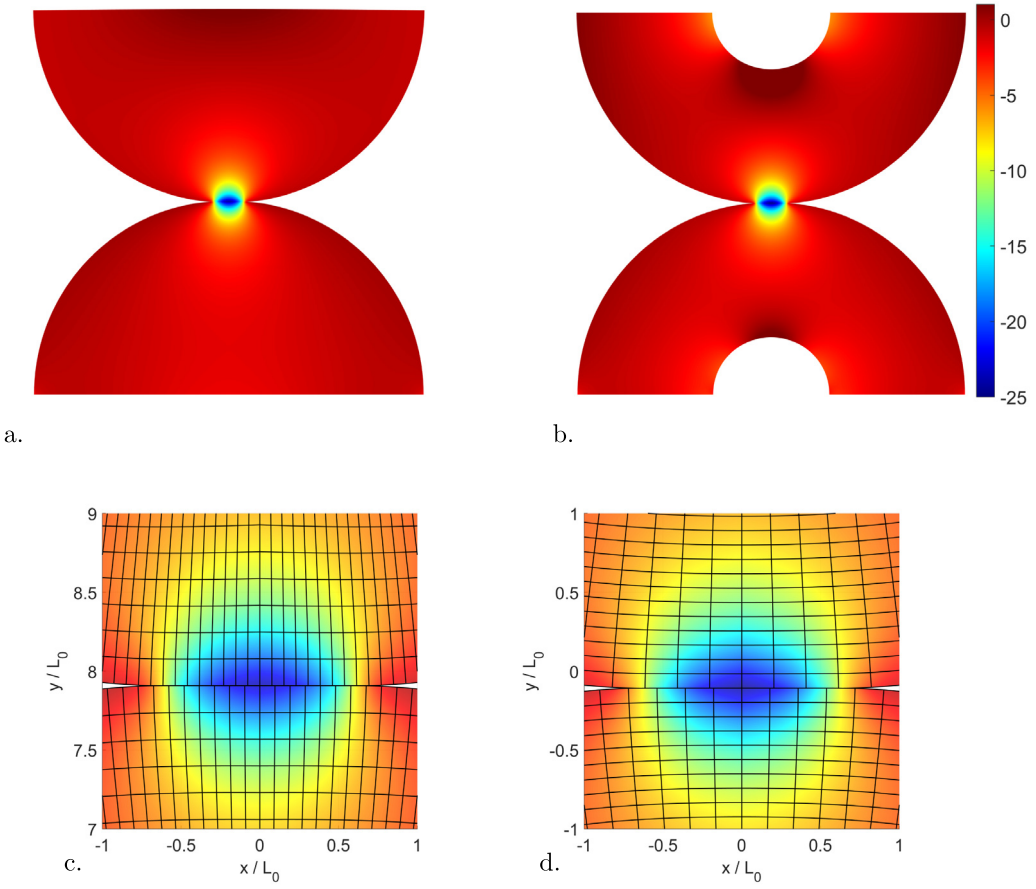


**Fig. 3.** Numerical solution of the Hertz contact problem: deformed configuration colored with the first stress invariant for (a.) Q1N2 mesh, and (b.) IGA mesh. A zoom in to the contact zone is also shown in (c–d.) for the two meshes at the refinement level of 192-Q1N2/128-IGA contact elements, respectively. Here for visualization, the full model is obtained from reflection of the computed symmetry model. (For interpretation of the references to color in this figure legend, the reader is referred to the web version of this article.)

Fig. 4a–b depicts the distribution of the true contact pressure (i.e. $\lambda/J_s$ where $J_s := \sqrt{\det[a_{\alpha\beta}]}/\sqrt{\det[A_{\alpha\beta}]}$ denotes the contact surface stretch) including the comparison to the analytical solution (see, e.g. [39]). As the figure shows, the solutions for both Q1N2 and IGA meshes are in good agreement with the analytical solution. For coarse mesh, however, some oscillation in the contact pressure is observed as seen in Fig. 4a, but it becomes smooth with mesh refinement as Fig. 4b shows. It can also be seen from Fig. 5a that, due to the assumption of small contact area used in the Hertz solution, the computed contact pressure is closer to the analytical solution in the small load case than in the larger one.

Fig. 5b shows the convergence of the peak contact pressure over mesh refinement. The error here is measured with respect to solutions with a fine mesh. With this, the convergence rate of around 2 and 1.6 is observed for the quadratic IGA mesh and Q1N2 mesh, respectively.

**Remark 7.1.** It should be noted that the obtained solutions in this example for MIP and STD are identical, which is to be expected since the formulations are identical for the residual vector.

**Remark 7.2.** The NURBS-enriched finite element (Q1N2) of Corbett and Sauer [16], see element (E) in Fig. 2c., should not be confused with the so-called NURBS-enhanced finite element, see e.g. [40]. The Q1N2 element here provides a transition from the bulk toward the smooth NURBS surface. Its shape functions $\mathbf{N}_e(\boldsymbol{\xi})$ are constructed

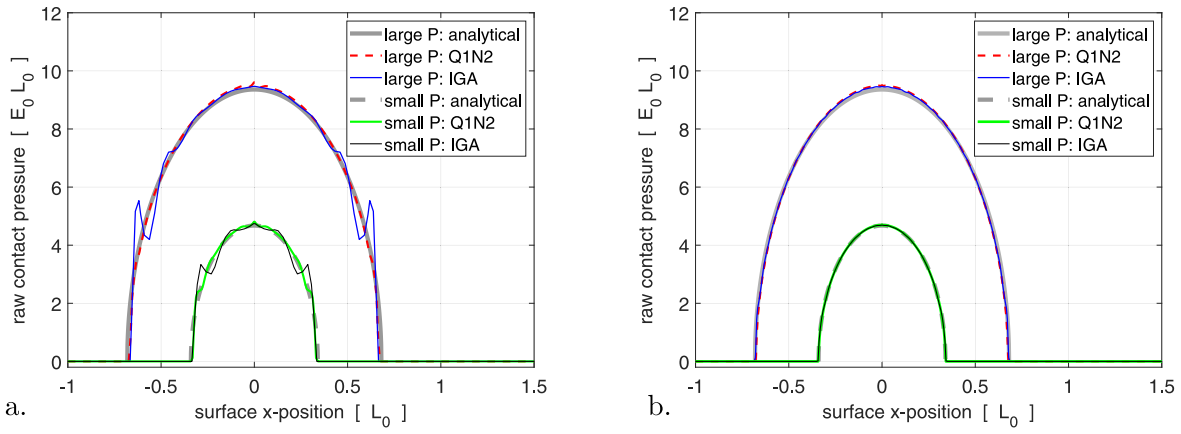


**Fig. 4.** Hertz contact: true contact pressure at integration points for (a.) coarse mesh (96-Q1N2/64-IGA contact elements) and (b.) fine mesh (384-Q1N2/256-IGA contact elements), considering the two discretization schemes and the two load levels.

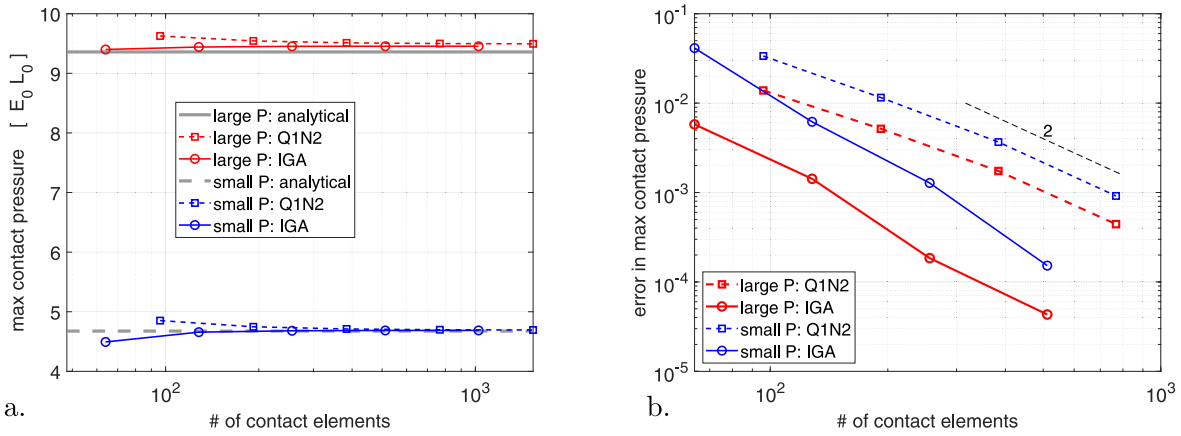


**Fig. 5.** Hertz contact: mesh convergence of the peak (true) contact pressure with respect to (a.) the Hertz's analytical solution and (b.) the numerical solution with the fine mesh (around 1.3 million dofs in the symmetry model, or 1536 contact elements on the slave surface).

consistently from the partition of unity condition and are able to interpolate any quantities, e.g position $\boldsymbol{x}$, in the same manner as Lagrangian elements (L), like $\boldsymbol{x} = \mathbf{N}_e(\boldsymbol{\xi})\,\mathbf{x}_e$, where $\mathbf{x}_e$ denote elemental nodal/control point positions.

### 7.2. *Contact patch test*

The second example further investigates the accuracy aspect of the MIP contact formulation via the so-called contact patch test. Since the contact residual vector of MIP contact is identical to the STD contact, it is expected here that the MIP contact formulation also passes all the contact patch tests like in STD.

To confirm this, we consider the three test cases as shown in Fig. 6a–c. To test our contact formulation for various element types, the upper bodies are described by the NURBS-enriched (Q1N2) finite elements of Corbett and Sauer [16], see Remark 7.2. The lower bodies are discretized by isogeometric elements with quadratic NURBS. The plane strain Neo-Hookean model (see e.g. [37]) is used with $E = 2\,E_0$ and $\nu = 0.3$. The penalty parameter for contact is $\epsilon = 10^2\,E_0/L_0$. A distributed external force $\boldsymbol{p} = -p\,\boldsymbol{n}$, with pressure $p = E_0\,L_0$ per current area and $\boldsymbol{n}$ being the edge normal vector, is applied to the (free) upper edges of the contact bodies.

Here, test case #1 shown in Fig. 6a is to check if the MIP formulation is able to transfer stress from one body to the other exactly through the contact interface. Test cases #2 and #3 additionally account for errors in numerical integration resolving the *artificial discontinuities* within the contact zone (Fig. 6b.) and the *physical discontinuities*

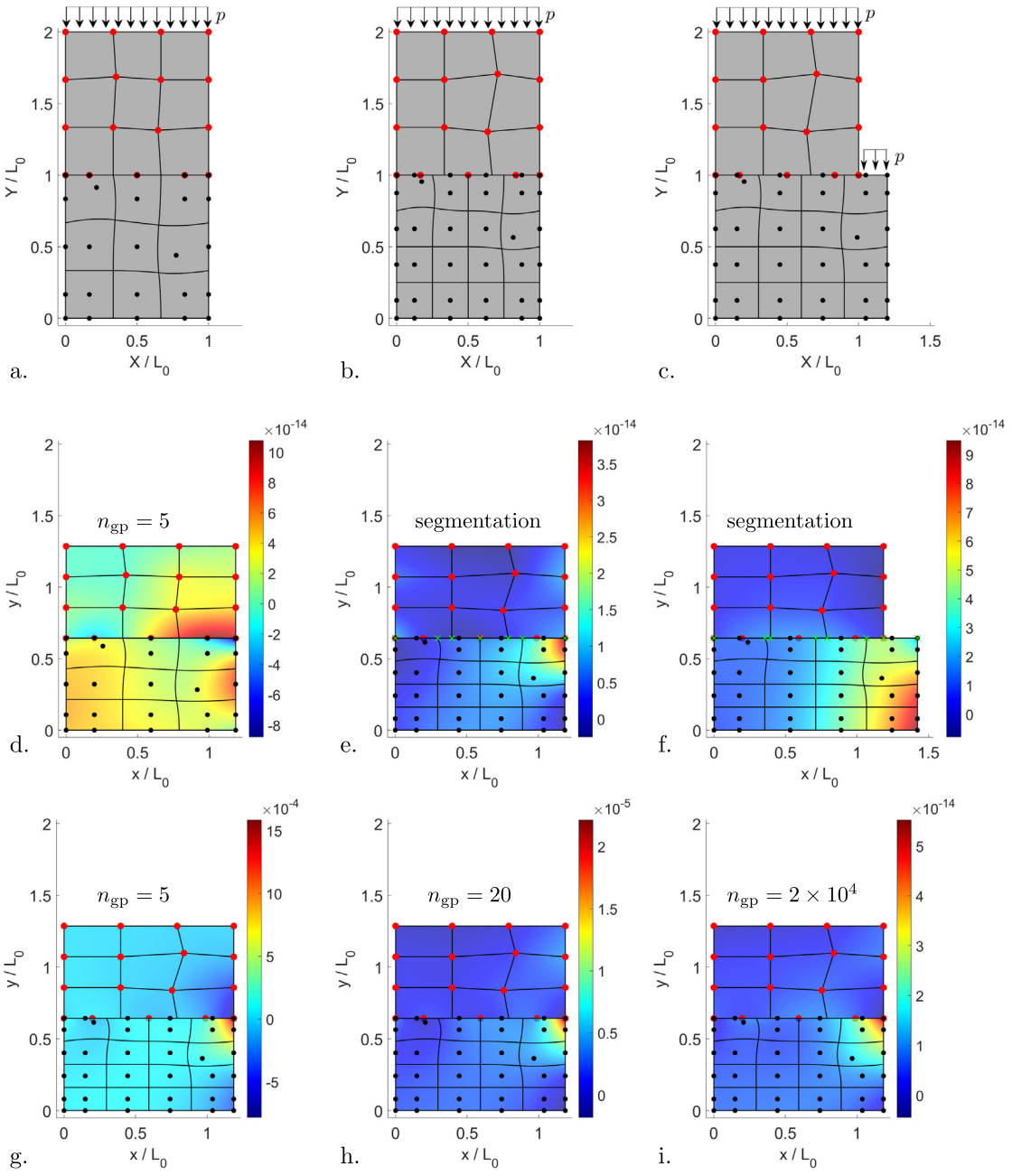


**Fig. 6.** Contact patch tests of MIP contact considering (a.) case #1: conforming mesh, (b.) case #2: non-conforming mesh, and (c.) case #3: generalized contact at the initial configuration. Here, the red and black bullets denote the nodes or control points of the upper and lower bodies, respectively. The nodes or control points at $X = 0$ and $Y = 0$ are fixed in the $x$-direction and in the $y$-direction, respectively. Further, the deformed configurations for test cases #1–3. are shown in (d–f.), respectively. The coloring shows the error in the vertical (true) stress. In (e–f.), the green crosses mark the intersecting points from the segmentation procedure for numerical integration with 5 Gauss points per segment. Case #2 is further tested with (g.) 5 Gauss points, (h.) 20 Gauss points, and (i.) $2 \times 10^4$ Gauss points per elements.. (For interpretation of the references to color in this figure legend, the reader is referred to the web version of this article.)

at the partial contact element (Fig. 6c), respectively. Like in mortar methods, e.g. [3], such discontinuities appear in the residual vector on the master surface Eq. ((49).2). Therefore, a proper numerical integration is required here in order to pass the tests to machine precision.

Fig. 6d–f. shows the testing results of the three test cases for the MIP contact, where a segmentation procedure (with 5 Gauss point per segment) is employed for the test cases #2–3. As seen, all the tests are passed to machine precision.

We further note that, since a smooth discretization for the contact surfaces is used in the test, the *artificial discontinuities* within the contact zone from Eq. ((49).2) are of the weak type. This implies that instead of the segmentation, many integration points can be used as an alternative in order to pass the patch test #2. This is demonstrated in Fig. 6g–i. where error in stress goes to machine precision with $2 \times 10^4$ Gauss points per element.

On the other hand at the edge contact like in case #3, where the upper contact surface is assigned as master, the many integration point approach is well-known to be ineffective due to the strong *physical discontinuities* there. In many contact simulations, one can bypass such discontinuities simply by switching the slave–master role in order to avoid an edge projection (see e.g. in the subsequent examples 7.5 and 7.6). In general, however, a consistent segmentation procedure is required there in order to ensure the robustness of contact simulations in general contact scenario.

### 7.3. Ironing in 2D: assessment of robustness of the MIP contact formulation

This section assesses robustness of the proposed MIP contact formulation in comparison with the STD contact formulation of Fischer and Wriggers [18] by considering the ironing example of a cylinder on a slab as shown in Fig. 7. Here, we will use the success flag – i.e. indication of a simulation completed without any convergence issue – as a robustness measure for the two considered contact methods.

Fig. 7a shows the initial (stress-free) configuration before contact is activated, where the cylinder with radius $R = L_0$ is pre-penetrated[4] by $0.01\,L_0$ into the slab of dimensions $5 \times 1\,L_0^2$. By employing the so-called NURBS-enriched finite elements of Corbett and Sauer [16,17], the contact surfaces are discretized by quadratic NURBS, while linear elements are used for the bulk. Since we aim at characterizing the robustness from the initial contact phase with a relatively small contact area, 20 Gauss points per element are used in our contact simulations. The plane strain Neo-Hookean model (see e.g. [37]) is used for both the cylinder ($E = 10\,E_0\ ,\ \nu = 0.3$) and the slab ($E = 2\,E_0\ ,\ \nu = 0.3$).

We consider the contact problem for various load step sizes and penalty parameters at the three distinct phases:

• **Initial contact**, see Fig. 7b: From the initial configuration, the cylinder is further pressed into the slab by applying a vertical displacement $u_y^0$ in a single load increment to the top control points (and nodes) of the cylinder. This phase is characterized by a small contact zone with relatively few integration points involved in contact. The numerical integration is usually inaccurate and thus induces difficulty in convergence of Newton iterations. Here we simulate this phase for various displacements $u_y^0$ and penalty parameters.

• **Pressing phase**, see Fig. 7c: this phase starts from a configuration converged at the end of the initial contact phase with $u_y^0 = -0.005\,L_0$ and $\epsilon = 500\,E_0/L_0$.[5] The cylinder is further displaced downward by $u_y = 0.5\,L_0$ for various load step sizes and penalty parameters, see Fig. 7c. Therefore, the contact zone is expanding and the active-set is expected to be updated frequently over the deformation.

• **Sliding phase**, see Fig. 7d: the simulation starts from a configuration converged at the end of the pressing phase with $\epsilon = 500\,E_0/L_0$. This phase aims at testing the contact formulation for large sliding contact. To this end, the cylinder is now displaced horizontally by $u_x = L_0$, also for various step sizes and penalty parameters. The applied displacement is also prescribed to the top control points (and nodes) of the cylinder.

Fig. 8a. shows that the load–displacement curves resulting from STD and MIP are identical. This is due to the fact that the two formulations have the same residual, as noted in Remark 6.3. Given a load increment with the same load step size, the convergence rate of the Newton-iterations for MIP and STD are almost identical as Fig. 8b shows.

Fig. 9 plots the success flag of the simulations for the standard penalty (displacement-based) contact formulation (STD) versus the presented MIP contact formulation at the three contact phases. At the initial contact phase, MIP is slightly more robust than STD at larger penalty parameter zone, while no improvement is observed at the pressing phase. This is shown in Fig. 9a–b, respectively.

[4] The pre-penetration here is merely to provide an initial guess for contact simulations once it is activated at the first load step.

[5] I.e. the initial contact simulation with the given $u_y^0$ and $\epsilon$ becomes the first part of pressing phase loading.

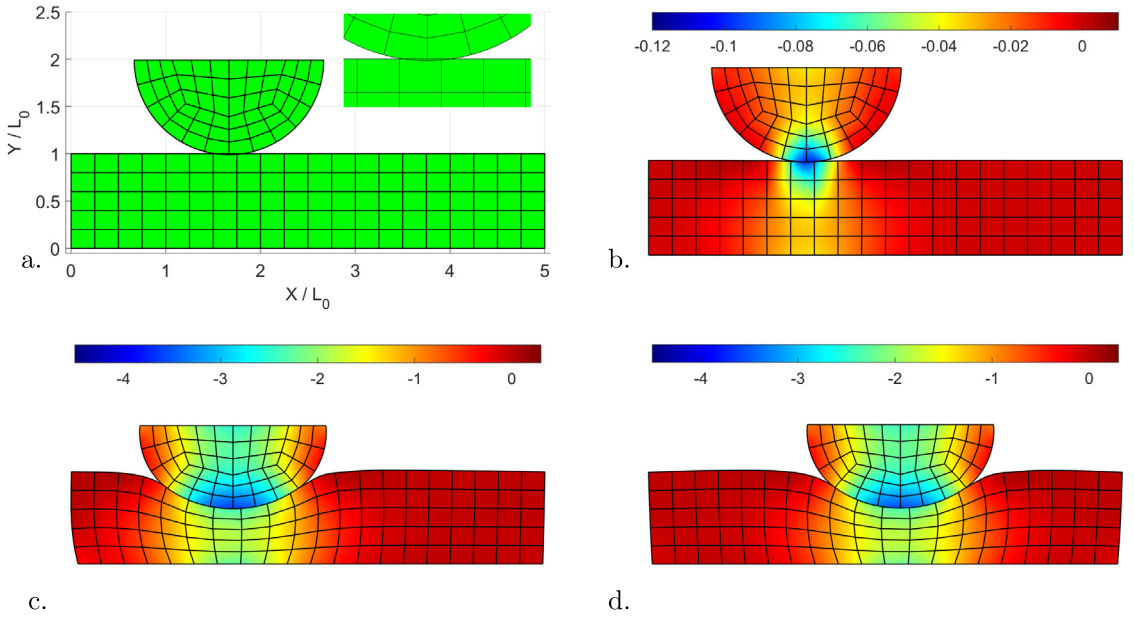


**Fig. 7.** Ironing of a cylinder block: a. Initial configuration with the pre-penetration $0.01\,L_0$ before contact is activated, and deformed configurations at the end of b. initial contact phase, c. pressing phase, and d. sliding phase. The color shows the first stress invariant. (For interpretation of the references to color in this figure legend, the reader is referred to the web version of this article.)

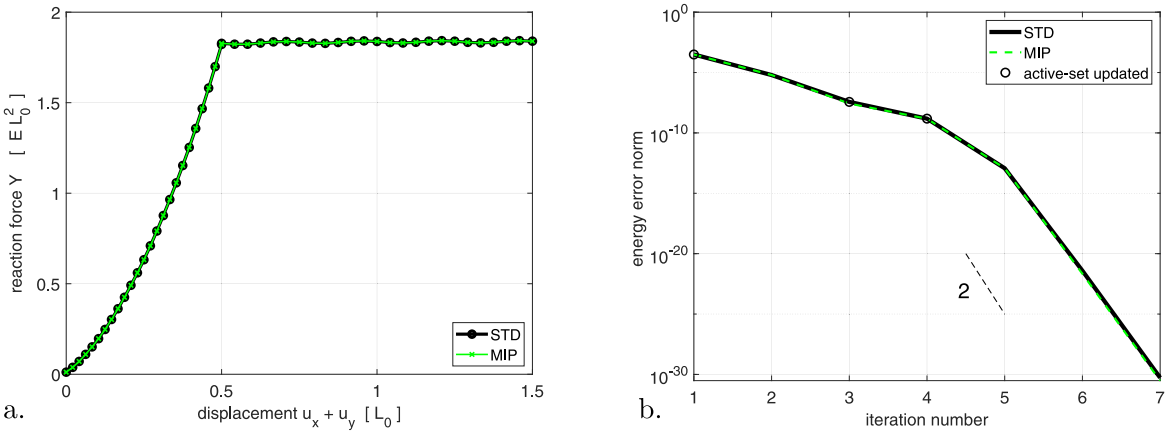


**Fig. 8.** Ironing of a cylinder block: a. load–displacement curves at the pressing and sliding phases and b. convergence of Newton iterations at the initial contact phase for STD versus MIP formulation with load step size $-0.0255\,L_0$. Here, $\epsilon = 500\,E_0/L_0$.

However, as Fig. 9c shows at the sliding phase, MIP significantly improves robustness of the contact simulation over STD for both larger load step sizes and larger penalty parameters. This implies that MIP offers more efficiency (since we can use larger step size), and more accurate constraint enforcement (since larger penalty parameters can be used).

**Remark 7.3.** The similarity of the convergence rate in STD and MIP shown Fig. 8b implies that numbers of iterations over the load increment of the two methods are more or less equal. However, MIP is still more efficient than STD since the improved robustness allows MIP for using a larger load step size. It also should be noted that MIP improves the robustness more significantly at the sliding phase than the initial contact and the pressing phase, as is seen from Fig. 9. Therefore, an adaptive load-stepping scheme usually improves the overall robustness and

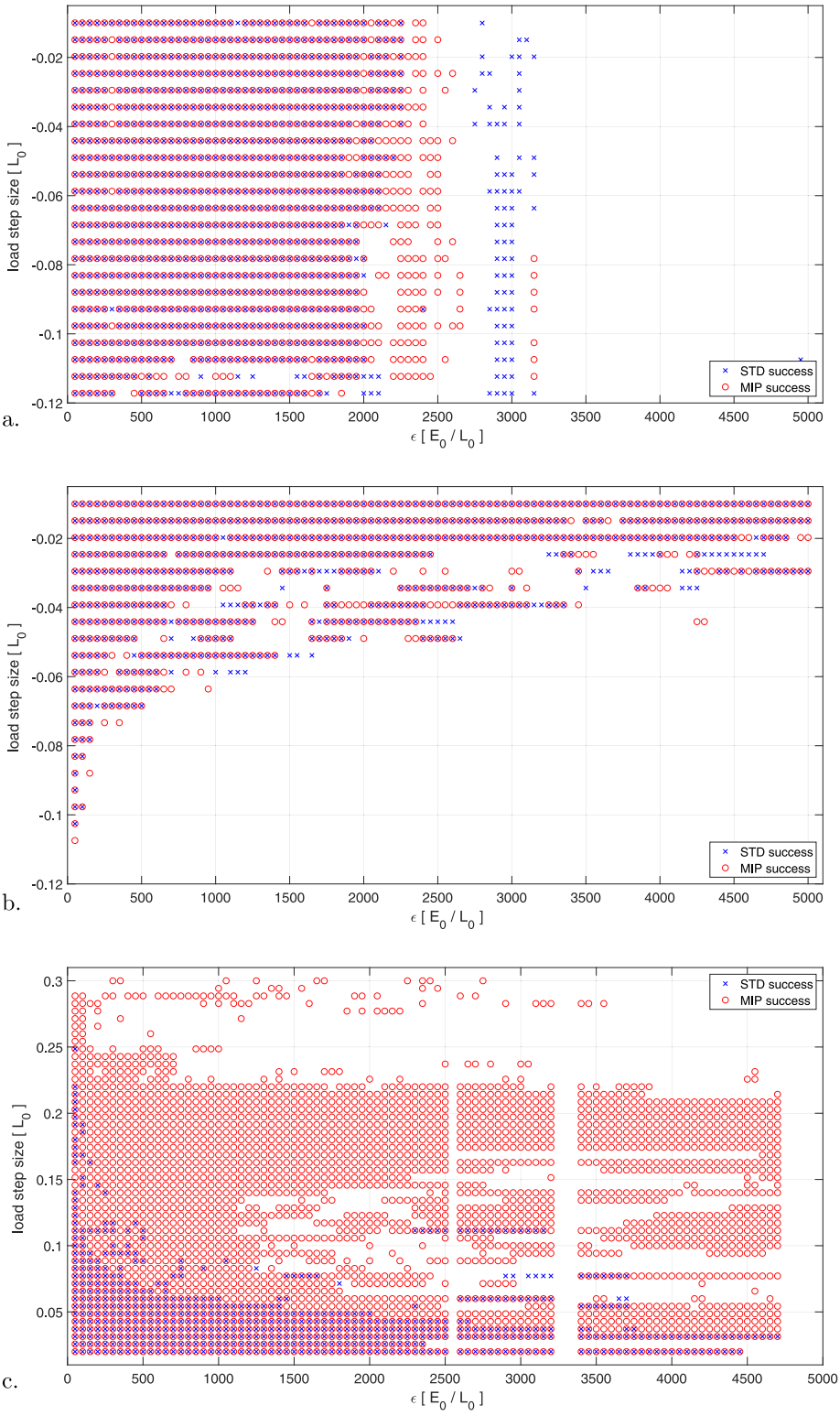


**Fig. 9.** Ironing of a cylinder block: successful flag of simulations using the standard penalty (displacement-based) contact formulation (STD) in comparison with the presented mixed interpolation point contact formulation (MIP) for various load-step sizes and penalty parameters at a. initial contact phase, b. pressing phase, and c. sliding phase.

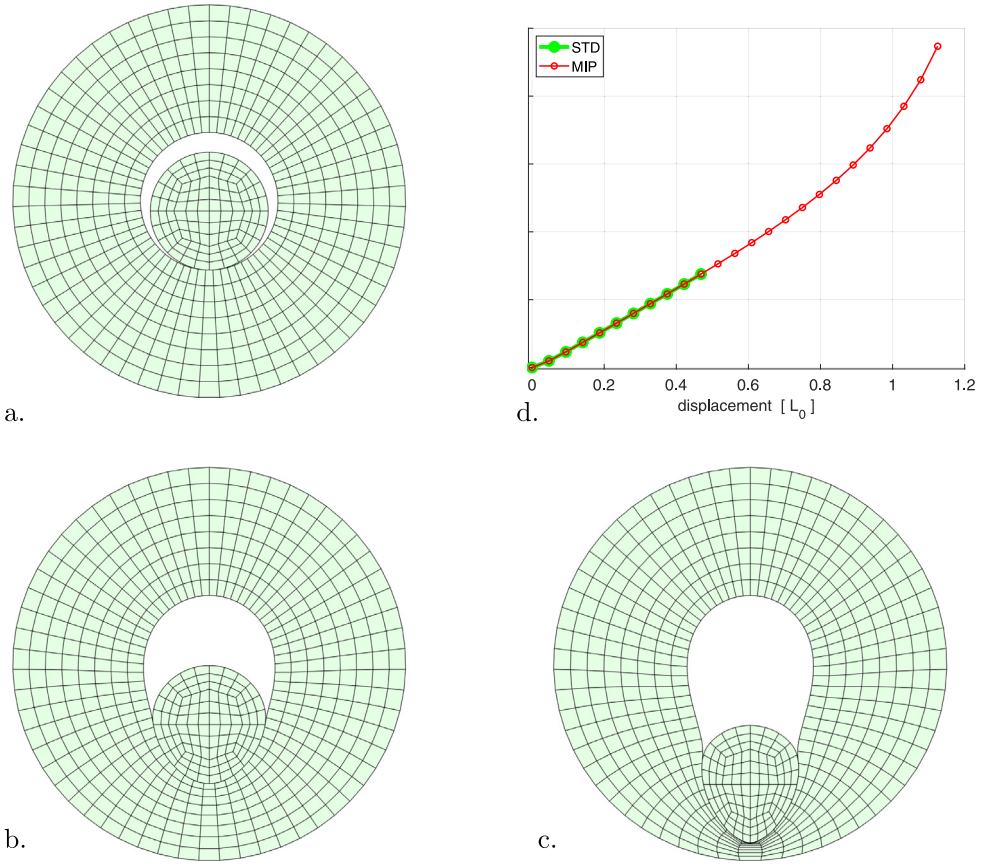


**Fig. 10.** Disc in a disc contact: Configurations at vertical displacements a. $0\,L_0$, b. $0.5156\,L_0$, and c. $1.125\,L_0$. d. Load–displacement curve for STD versus MIP contact. Here, $\epsilon = 5 \times 10^6\, E_0/L_0$ and 25 load increments are used. The STD formulation failed to converge at load step #12, while the proposed MIP finished simulation without convergence issue.

efficiency in sliding-dominated simulations. In this case, MIP contact often requires less number of load steps, or equivalently, requires less total number of Newton iterations over simulation. We will demonstrate the effectiveness of an adaptive load-stepping scheme in the examples 7.6 and 7.7.

### *7.4. Disc in a disc contact*

The next example simulates the 2D contact of a disc in a disc as shown in Fig. 10. A 3D version of this example was discussed in [3] to test a contact formulation for large deformation at the contact interface. The radius of the solid disc is taken as $r = 0.6\,L_0$, while $r_\mathrm{i} = 0.7\,L_0$, and $r_\mathrm{o} = 2\,L_0$ for the inner and outer radius of the hollow disc, respectively. We apply the plane strain Neo-Hookean material for both the solid disc ($E_\mathrm{s} = 2000\,E_0$ , $\nu_\mathrm{s} = 0.3$) and the hollow disc ($E_\mathrm{h} = 1000\,E_0$ , $\nu_\mathrm{h} = 0.0$). With the NURBS-enriched finite elements [16,17], the contact interfaces and the bulk are discretized by quadratic NURBS elements and linear Lagrange elements, respectively. The master surface is assigned to the boundary surface of the solid disc.

All control points at the outer boundary of the hollow disc are fixed. Starting from the initial configuration shown in Fig. 10a, the total displacement $u_y = -1.125\,L_0$ is prescribed on the vertical degrees of freedom of all control points (and nodes) of the solid disc, while their horizontal degrees of freedom are kept free. Here, 25 load increments are used for the prescribed displacement.

We use a penalty parameter $\epsilon = 5 \times 10^6\, E_0/L_0$ and 20 Gauss points per element for the contact surface. With these parameters, MIP contact finished the simulation successfully, while STD contact fails to converge at load step #12.

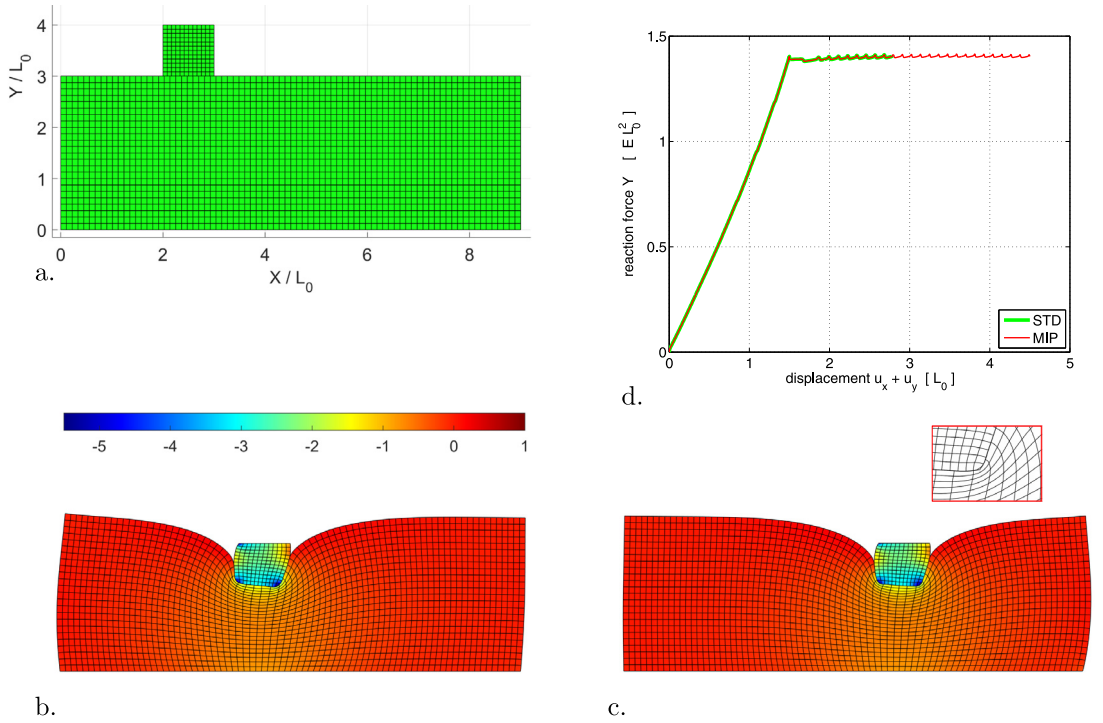


**Fig. 11.** Ironing of a square block: a. Initial configuration, b–c. deformed configurations at $\boldsymbol{u} = (-1.5,\ 0)\,L_0$ and $\boldsymbol{u} = (-1.5,\ 3)\,L_0$, respectively. The color shows the first stress invariant. d. load–displacement curve considering STD (standard) and MIP contact formulations for penalty parameter $\epsilon = 400 E_0/L_0$ and load step size $0.0043\,L_0$. Here, STD failed to converge at load #553, while MIP completed simulation without convergent issue. (For interpretation of the references to color in this figure legend, the reader is referred to the web version of this article.)

Fig. 10a–c plot several snapshots of the discs during the deformation. As seen from Fig. 10c at the area with the maximum contact pressure, the contact constraint is enforced quite accurately with the proposed MIP contact formulation, given that the solid disc undergoes large deformation there. Further, the large change in the contact area of the hollow disc results in a significant dissimilarity in mesh size between the slave and master meshes. The load–displacement curves are further plotted in Fig. 10d.

### *7.5. Ironing of a square block*

The fifth example considers the sliding of a square block pressed and slid on a slab surface as shown in Fig. 11. This problem is challenging for contact formulations due to the stress singularity at the corners of the block.

The dimensions of the block and the slab are $1\times1\,L_0^2$ and $9\times4\,L_0^2$, respectively. The block and slab are discretized by quadratic NURBS elements for both the bulk and contact surfaces. We assume the Neo-Hookean visco-hyperelastic material for the block ($E_\mathrm{b} = 5\,E_0\ ,\ \nu_\mathrm{b} = 0.3\ ,\ \eta_\mathrm{b} = 1$) and the slab ($E_\mathrm{s} = E_0\ ,\ \nu_\mathrm{s} = 0.3\ ,\ \eta_\mathrm{s} = 1$). Fig. 11a shows the initial configuration.

All the control points at the bottom of the slab are fixed. The displacement is applied at the control points on the top edge of the block. The block is first pressed into the slab by the vertical displacement $u_y = -1.5\,L_0$ with 250 load increments. It is then slid horizontally up to a displacement $u_x = 3\,L_0$ with 700 load increments. The penalty parameter $\epsilon = 400\,E_0/L_0$ is taken for the contact.

With the above parameters, MIP contact can finish the simulation successfully, while STD contact failed to converge at load step #553. Fig. 11b–c. show the configurations at the end of the pressing step and the sliding step, respectively. As seen, although the contact surface of the slab is stretched significantly (inducing a significant dissimilarity in mesh size), the contact constraint is still fulfilled quite accurately. During the sliding, the reaction

force is oscillating as shown in Fig. 11d. The picks of the oscillation can be seen to be corresponding to the contact of the block corners crossing over the contact element boundaries of the slab.

### 7.6. Ironing in 3D of a cylinder on a block

This example considers the ironing problem in 3D of a cylinder on a block, which was discussed in [3] for mortar methods. Using the adaptive load-stepping scheme in Appendix B, we further demonstrate the efficiency of the proposed MIP contact, which benefits from its enhanced robustness as discussed in Section 7.3.

The considered example is similar to the 2D example in Section 7.3 but we model the cylinder now with the Kirchhoff–Love shell element of Kiendl et al. [41] as shown in Fig. 12. Here, both the cylinder and the block are discretized by the quadratic NURBS elements. We consider three different meshes as seen in Fig. 12a.

The model parameters are taken from Puso and Laursen [3]. That is, the dimensions of the cylinder is $R = 3\,L_0$, $T = 0.3\,L_0$ thick, and $L = 5.3\,L_0$ long, and its material parameters are ($E_\mathrm{c} = 1000\,E_0$ , $\nu_\mathrm{c} = 0.3$) for the shell model. The dimensions of the slab is $9 \times 4 \times 3\,L_0^2$, its material is Neo-Hookean hyperelasticity with ($E_\mathrm{b} = 1\,E_0$ , $\nu_\mathrm{b} = 0.3$). The master surface is assigned for the cylinder.

The bottom-most control points of the block are fixed in all directions. The cylinder is pressed downward by prescribing the vertical displacement $\bar{u}_z = 1.4\,L_0$ on its topmost control points. It is then slid horizontally by prescribing the displacement $\bar{u}_x = 4\,L_0$ (also on the topmost control points) in the $x$-direction. Various penalty parameters $\epsilon = \{500,\ 1000,\ 1500,\ 2000\}E_0/L_0$ are used. We further employ the adaptive load-stepping scheme described in Appendix B in order to maximize the benefit from the robustness advantage of the MIP contact method, see also Remark 7.3. We take the load-stepping parameters: $\Delta\bar{u}_z^{\min} = 0.01\,L_0$, $\Delta\bar{u}_z^{\max} = 0.035\,L_0$, $\Delta\bar{u}_z^{\text{suggested}} = 0.01\,L_0$, $\Delta\bar{u}_x^{\min} = 0.02\,L_0$, $\Delta\bar{u}_x^{\max} = 0.0667\,L_0$, $\Delta\bar{u}_x^{\text{suggested}} = 0.02\,L_0$. The expected number of iteration per load step is $N_\mathrm{e} = 9$ for the pressing phase, and $N_\mathrm{e} = 10$ for the sliding phase, accounting for active-set update iterations.

Fig. 12b–c. shows several snapshots of the converged configurations for the three meshes. As Fig. 12d. shows, the contact constraint as well as the deformation at the contact area are seen to be quite accurate even for a very coarse mesh. Also, the load–displacement curve is plotted in Fig. 13a, which shows a smooth behavior of contact. This reflects the effectiveness of the isogeometric discretization.

In order to measure the efficiency of the considered contact formulations using the adaptive load-stepping scheme, we use the accumulated number of Newton iterations over the simulation. Such iteration count is plotted Fig. 13b for the standard penalty-based (STD) contact versus the proposed MIP contact method, considering various penalty parameters. As can be seen, the iteration count for STD contact and MIP contact is of the same order at the pressing phase. But at the sliding phase, MIP needs much fewer iterations than STD, corresponding to higher efficiency of the algorithm. This is due to larger load step sizes allowed (and thus less number of load steps required) for MIP, although the rate of convergence of Newton iteration per load step is almost unchanged with respect to STD. This figure once more confirms the assessment in Section 7.3.

**Remark 7.4.** It should be noted that if the master surface is assigned to the block instead of the cylinder here, a divergence of Newton iterations is expected since a projection on the edges of the block appears in this case. As discussed in [1], in principle a segmentation at boundaries of the contact zone is required to resolve the numerical integration there. E.g. a so-called refined boundary quadrature techniques (RBQ) proposed by Duong and Sauer [19] can be employed for this purpose.

### 7.7. Inflated balloon in elastic tube

This section presents the last example testing the contact formulations with inflating a balloon inside an elastic tube, which is inspired from angioplasty. We also investigate the efficiency gain of MIP over STD formulation with the adaptive load-stepping scheme in Appendix B.

The initial configurations of both the balloon and the tube are in the cylindrical shape, which are discretized by quadratic NURBS elements as shown in Fig. 14a-d. Their radii and (overall) lengths are $R_\text{balloon} = 0.5\,L_0$, $L_\text{balloon} = 5.5\,L_0$, $R_\text{tube} = L_0$, $L_\text{tube} = 24\,L_0$. The balloon is initially positioned at the distance $13.7\,L_0$ from the right end of the tube. The left end of the balloon is closed with the hemisphere of radius $0.5\,L_0$.

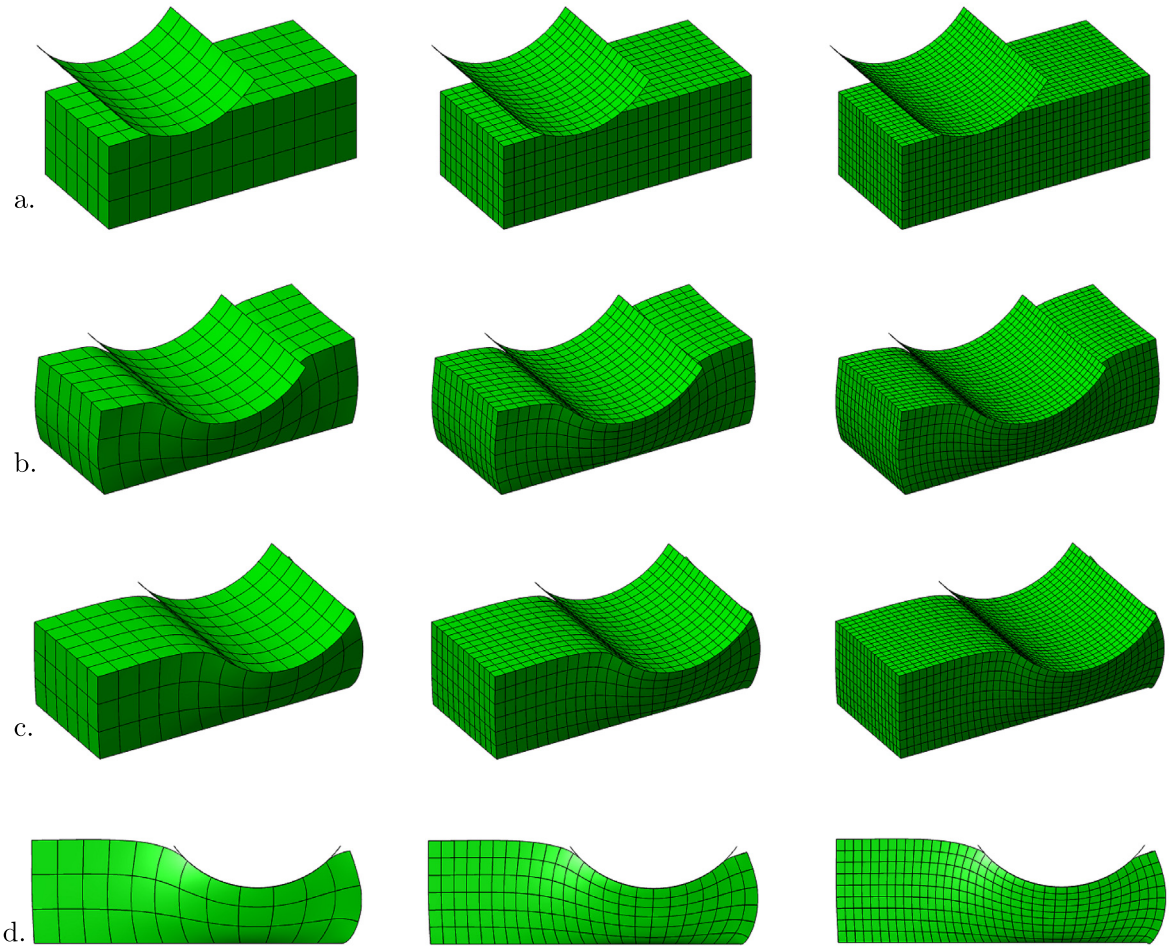


**Fig. 12.** Ironing of a 3D cylinder: rows a–c. plot configurations in a 3D view at prescribed displacement $\boldsymbol{u} = (0,\ 0)\, L_0$, $\boldsymbol{u} = (-1.4,\ 2.03)\, L_0$ and $\boldsymbol{u} = (-1.4,\ 4)\, L_0$, respectively, considering three different meshes (from left to right): mesh #1 (280 elements), mesh #2 (1984 elements), and mesh #3 (6408 elements). Row d. plots configuration in a side view at $\boldsymbol{u} = (-1.4,\ 4)\, L_0$ for the considered meshes. Here, the penalty parameter is $\epsilon = 1000 E_0/L_0$.

The balloon inflation is done here by constraining the enclosed volume of the balloon, denoted by $V$, using the surface potential as, see [42]

$$\Pi_{\mathrm{v}} = p\,(V - V_{\mathrm{prescribed}})\ , \tag{50}$$

where $p$ is the Lagrange multiplier (additional unknown) with the physical meaning of the internal pressure acting on the balloon wall, and $V_{\mathrm{prescribed}}$ denotes the externally prescribed volume, corresponding to a desired volume of air filled into the balloon.

In the example, the balloon and the tube are modeled by the Kirchhoff–Love shell [43] with the membrane and bending responses

$$\begin{aligned} \tau^{\alpha\beta} &= \mu\left(A^{\alpha\beta} - \frac{a^{\alpha\beta}}{J^2}\right) + \frac{1}{2}\,\Lambda\,(J^2-1)\,a^{\alpha\beta}\ , \\ M_0^{\alpha\beta} &= c\,A^{\alpha\gamma}\,(b_{\gamma\delta} - B_{\gamma\delta})\,A^{\delta\beta}\ , \end{aligned} \tag{51}$$

of Sauer et al. [42] and Zimmermann et al. [44], respectively. Here, $a^{\alpha\beta}$ and $b_{\alpha\beta}$ are the components of the membrane (or shell) surface metric and the surface curvature tensors, respectively, while $A^{\alpha\beta}$ and $B_{\alpha\beta}$ denote the corresponding

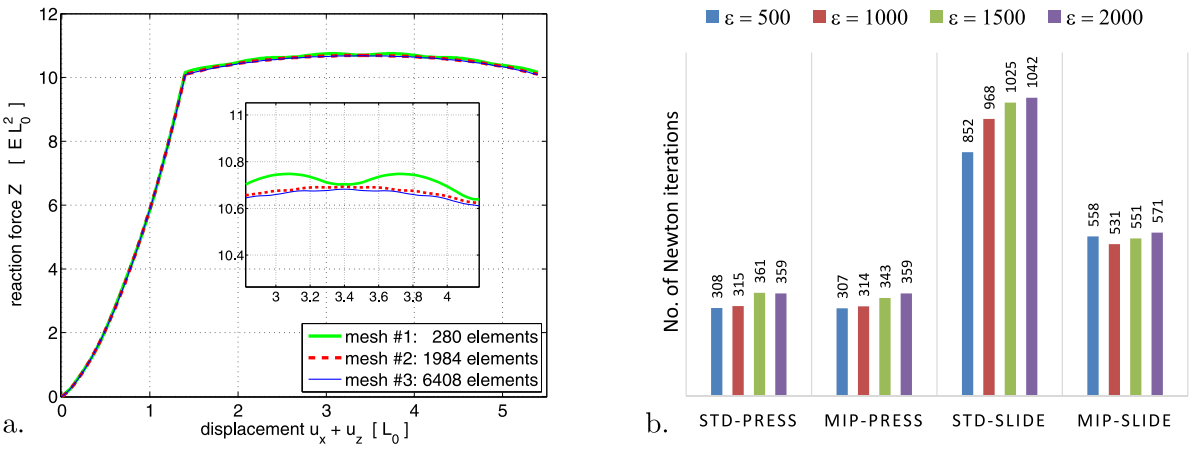


**Fig. 13.** Ironing of a 3D cylinder: a. load–displacement curves for different meshes with $\epsilon = 1000 E_0/L_0$. b. Comparison of Newton iteration counts for the standard penalty-based contact (STD) and proposed MIP contact. Here, we use mesh #1 (280 elements) with the adaptive load stepping scheme in Appendix B for various penalty parameters $\epsilon$.

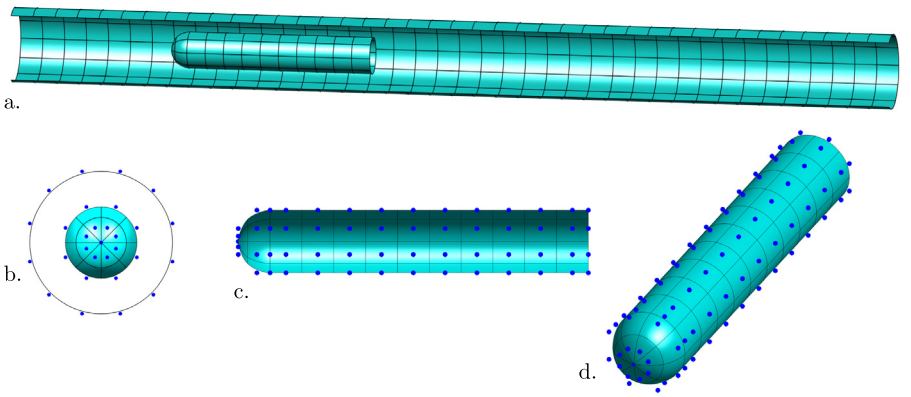


**Fig. 14.** Inflated balloon in elastic tube: Initial mesh showing (a.) the balloon inside the tube. (b.) zoom in the left-side view of (a.) with the control points represented by blue dots, (c.) front view and (d.) 3D view of the balloon. The tube is meshed with a single NURBS patch, while the balloon is meshed with two NURBS patches for its cylindrical body and the hemispherical cap, respectively. For both the balloon and the tube, $C^1$-continuity is ensured along their circumferences.

quantities in the reference configuration. $J$ denotes the surface stretch, and $\mu$, $\Lambda$, and $c$ are material parameters. In the example, we set $\mu = 1\, E_0/L_0$, $\Lambda = 1\, E_0/L_0$ for both the balloon and the tube, while $c_{\text{balloon}} = 0$ (i.e. no bending stiffness) and $c_{\text{tube}} = 0.1\, E_0\, L_0$.

For simulations, the left end of the tube is fixed in all directions, while its right end is fixed in the radial directions leaving the axial direction free. We use $3 \times 3$ Gauss points per either a contact or a membrane/shell element. The simulation starts with inflating the balloon within a pseudo time unit by applying $V_{\text{prescribed}} = \bar{\alpha}_{\text{v}}\, V_0$, with $\bar{\alpha}_{\text{v}} = 40$ and $V_0$ being the initial volume. During the inflation, the right end of the balloon is fixed in all directions. Within another pseudo time unit, the inflated balloon is then slid on the tube wall by prescribing the displacement $\bar{u}_x = 11.5\, L_0$ on the right end of the balloon in the axial direction. The adaptive load-stepping parameters for the inflation phase are $\Delta\bar{\alpha}_{\text{v}}^{\min} = \bar{\alpha}_{\text{v}}/500$, $\Delta\bar{\alpha}_{\text{v}}^{\max} = \bar{\alpha}_{\text{v}}/15$, $\Delta\bar{\alpha}_{\text{v}}^{\text{suggested}} = \bar{\alpha}_{\text{v}}/150$. For the sliding phase, the load-stepping parameters are $\Delta\bar{u}_x^{\min} = \bar{u}_x/500\, L_0$, $\Delta\bar{u}_x^{\max} = \bar{u}_x/25\, L_0$, and $\Delta\bar{u}_x^{\text{suggested}} = \bar{u}_x/350\, L_0$.

Fig. 15a–f show several snapshots of the simulation. The internal pressure on the balloon wall (i.e. the Lagrange multiplier from the volume constraint) over time is plotted in Fig. 16a. As expected, identical results are obtained from STD and MIP.

Further, in order to investigate the influence of the adaptive load stepping scheme on the efficiency of simulations, we define a so-called efficiency gain of MIP $e_{\text{mip}}$ as

$$e_{\text{mip}} := \frac{n_{\text{iters}}^{\text{std}} - n_{\text{iters}}^{\text{mip}}}{n_{\text{iters}}^{\text{std}}} \times 100\% \ , \tag{52}$$

where $n_{\text{iters}}^{\bullet}$ denotes the accumulated number of Newton iterations. Fig. 16b plots the efficiency gain considering various penalty parameters and various adaptive load-stepping parameters $N_{\text{e}}$, the expected numbers of iterations. It should be noted that the parameter $N_{\text{e}}$ is a user-defined parameter that controls the "sensitivity" of the adaptive load-stepping algorithm to alter the load step size for the current load step. It is simply based on a relative difference between the given parameter $N_{\text{e}}$ and the actual number of iterations in the previous load step, see Eq. (58).

As Fig. 16b shows, there exists an optimal value of penalty parameter that maximizes the efficiency of MIP for each parameter $N_{\text{e}}$. In particular for the low parameter $N_{\text{e}} = 6$, the efficiency gain of MIP is below 20%. It can also be seen that at the range of high penalty parameters e.g. $\epsilon = 600\, E_0/L_0$, MIP can lose the efficiency by about 20% with $N_{\text{e}} = 11$. However, in most of the cases, MIP has a clear efficiency gain and for $N_{\text{e}} = 13$ with $\epsilon = 600\, E_0/L_0$, the efficiency gain is about 45% in the presented example, i.e. the total number of iterations is reduced to almost one half.

Fig. 17a–b show more details in the development of the accumulated number of iterations over time for several penalty parameters with a fixed $N_{\text{e}}$ and for several adaptive load-stepping parameters $N_{\text{e}}$ with a fixed penalty parameter, respectively. As seen from the figure, the efficiency of MIP has gained mainly from the sliding phase, which again confirms the assessment in Section 7.3.

## 8. Conclusion

In this work, we propose an application of the mixed interpolation point method (MIP) [22] to a displacement-based frictionless contact formulation in order to enhance its robustness and efficiency. We employ a smooth isogeometric discretization of contact surfaces to deal with the issues related to artificial discontinuities of the normal contact gap. The proposed MIP contact formulation is derived by first considering the contact pressure as an additional unknown field apart from the displacement field and a perturbed Lagrange multiplier potential enforces the contact constraint. While the displacement field is discretized as usual, the contact pressure is then solved directly at quadrature points by static condensation. Such treatment results in a reduced residual vector, which is identical to the standard penalty formulation. But the difference lies in the corresponding (reduced) tangent stiffness matrix, which is now required to extrapolate the contact pressure $\lambda$ for each iteration. The extrapolation here stems from the relaxation of the contact constitution $\lambda = \epsilon\, g_{\text{n}}$ (Eq. (16)) during iterations, but it is then satisfied at convergence. The properties of the MIP stiffness matrix, like symmetry and band width, are identical to those of the STD stiffness matrix.

As only few changes are required for the tangent matrices, an implementation of the proposed MIP contact formulation can be obtained by a minor modification from an existing code for the standard penalty formulation. The change turns out to improve the robustness over the standard penalty formulation quite significantly, as is demonstrated by the examples in Section 7. It is particularly effective during the sliding phase of contact problems as discussed in Section 7.3. The upgraded contact algorithm improves both efficiency and accuracy aspects of contact simulations, since it is usually shown to converge for a larger load step size and a larger penalty parameter in comparison with the standard penalty formulation. Consequently, an adaptive-load stepping scheme can facilitate the overall robustness and efficiency of simulations as demonstrated in the examples 7.6 and 7.7.

The presented MIP contact method, in principle, can be extended to a penalty-based mortar method, which enforces a weakened contact constraint function. Frictional contact problems – which can be treated similarly to an elasto-plasticity formulation – would be another important extension of the present work. These are left for future studies.

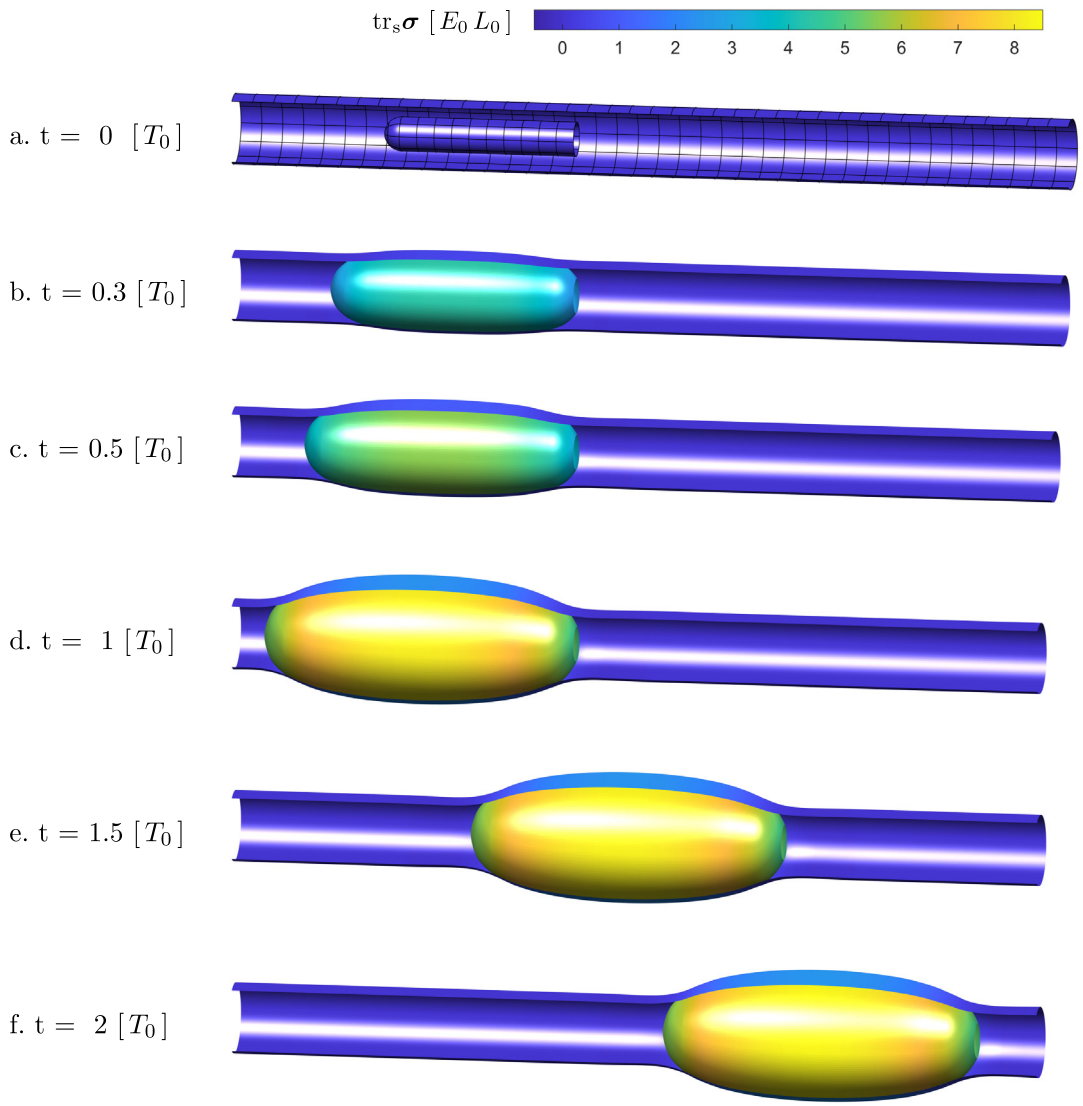


**Fig. 15.** Inflated balloon in elastic tube: configurations colored by the first stress invariant $I_1 = \mathrm{tr_s}\boldsymbol{\sigma}$ at various pseudo times $t$. Here, the penalty parameter $\epsilon = 600\, E_0/L_0$ is used. (For interpretation of the references to color in this figure legend, the reader is referred to the web version of this article.)

## Declaration of competing interest

The authors declare that they have no known competing financial interests or personal relationships that could have appeared to influence the work reported in this paper.

## Data availability

Data will be made available on request.

## Acknowledgments

This work has received funding from the European Research Council (ERC) under the European Union's Horizon 2020 research and innovation program (grant agreement No 864482) and from the Departments of Excellence project of the Italian Ministry of University and Research, which is gratefully acknowledged.

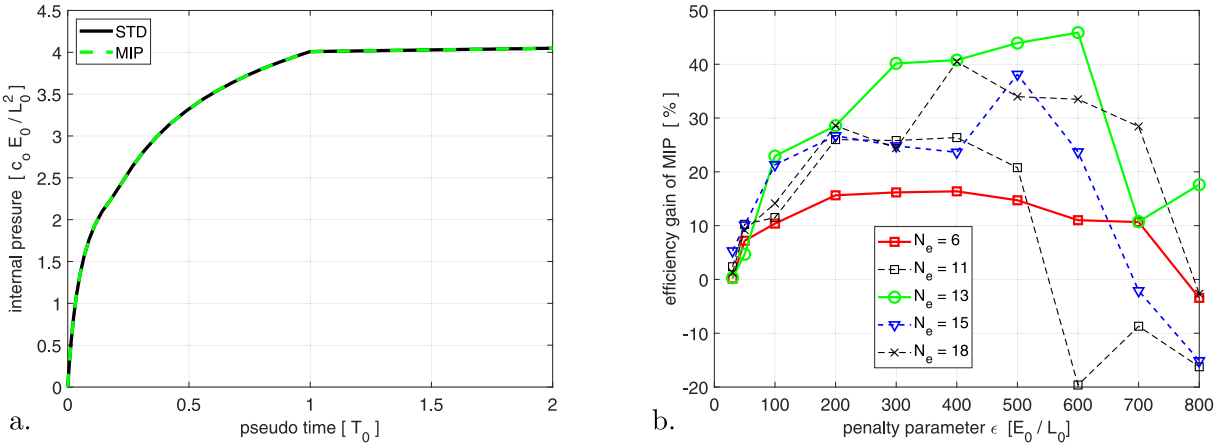


**Fig. 16.** Inflated balloon in elastic tube: a. internal pressure acting on the balloon wall over time. b. efficiency gain $e_{\text{mip}}$ (Eq. (52)) for various penalty parameters $\epsilon$ and various adaptive load-stepping parameters $N_{\text{e}}$.

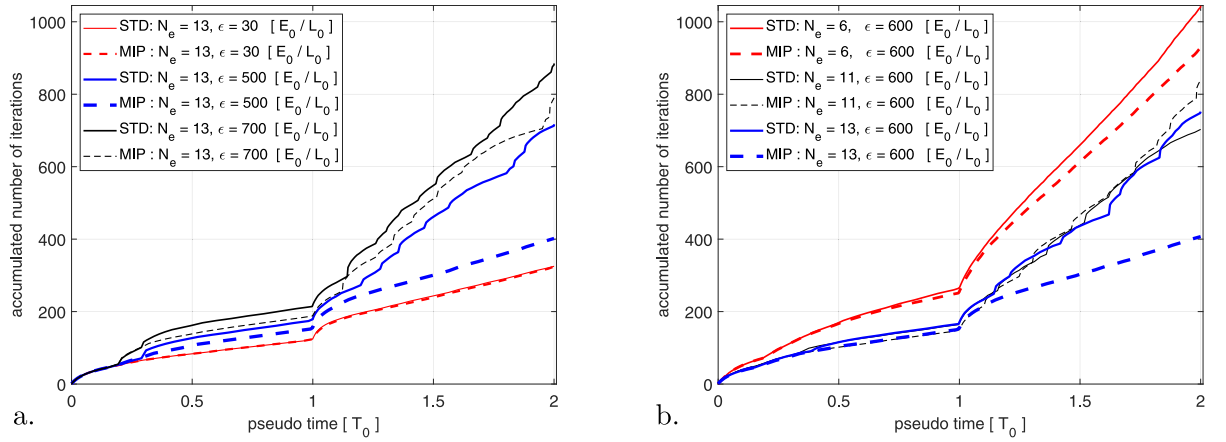


**Fig. 17.** Inflated balloon in elastic tube: accumulated number of Newton iterations over time for a. several penalty parameters $\epsilon$ at $N_{\text{e}} = 13$, and b. several adaptive load-stepping parameters $N_{\text{e}}$ at $\epsilon = 600\, E_0/L_0$.

## Appendix A. The standard penalty GPTS contact formulation

This appendix summarizes the finite element contact forces and the stiffness matrices of the penalty (pure displacement-based) contact formulation of Fischer and Wriggers [18]. According to De Lorenzis et al. [7], the formulation of Fischer and Wriggers [18] falls into the category of Gauss-point-to-segment (GPTS) methods since the contact constraint is enforced at each integration point. This is to distinguish from the mortar contact method proposed by Puso and Laursen [3], where the contact constraint is enforced weakly with a smoothed gap function. As discussed in Duong et al. [1] (cf. Sec. 3.4), the GPTS formulation of Fischer and Wriggers [18] and the mortar method of Puso and Laursen [3] can be unified in a so-called generalized mortar method, where different mortar shape functions with various degrees of weakness in the contact constraint enforcement can be employed.

The finite element contact residual according to Fischer and Wriggers [18] follows from Eq. (17) considering discretization (18) and (19) as

$$\delta \Pi_{\text{c}}(\mathbf{u}) = \delta\mathbf{u} \cdot \mathbf{r}_{\text{c}}(\mathbf{u}) = \underbrace{\begin{bmatrix} \delta\mathbf{x}_{\text{s}} \\ \delta\mathbf{x}_{\text{m}} \end{bmatrix}}_{\delta\mathbf{u}} \cdot \underbrace{\begin{bmatrix} \mathbf{r}_{\text{s}} \\ \mathbf{r}_{\text{m}} \end{bmatrix}}_{\mathbf{r}_{\text{c}}} = 0 \,, \qquad \text{for} \quad \forall \delta\mathbf{u} \in \mathcal{V}^h \,, \tag{53}$$

where $\mathcal{V}^h$ is now the kinematically admissible variations of the control points, and

$$\mathbf{r}_\mathrm{s} \;\coloneqq\; \sum_{i=1}^{a} \mathop{\mathbb{A}}_{e} \mathbf{N}_e^\mathrm{T}\, \boldsymbol{T}_\mathrm{c}\, w_i \;, \qquad \mathbf{r}_\mathrm{m} \coloneqq -\sum_{i=1}^{a} \mathop{\mathbb{A}}_{\hat{e}} \mathbf{N}_{\hat{e}}^\mathrm{T}\, \boldsymbol{T}_\mathrm{c}\, w_i \;, \qquad \text{and} \qquad \boldsymbol{T}_\mathrm{c} \coloneqq \epsilon\, g_\mathrm{n}\, \boldsymbol{n}_\mathrm{p} \;, \tag{54}$$

are the finite element contact forces acting on slave and master control points, and the (apparent) contact traction at integration point, respectively. The contact stiffness matrices can be obtained from the linearization of Eq. (53) and then rearranged as

$$\Delta\delta\, \Pi_\mathrm{c}(\mathbf{u}) = \underbrace{\begin{bmatrix} \delta\mathbf{x}_\mathrm{s} \\ \delta\mathbf{x}_\mathrm{m} \end{bmatrix}}_{\delta\mathbf{u}} \cdot \underbrace{\begin{bmatrix} \mathbf{k}_\mathrm{ss} & \mathbf{k}_\mathrm{sm} \\ \mathbf{k}_\mathrm{ms} & \mathbf{k}_\mathrm{mm} \end{bmatrix}}_{\mathbf{K}_\mathrm{c}} \underbrace{\begin{bmatrix} \Delta\mathbf{x}_\mathrm{s} \\ \Delta\mathbf{x}_\mathrm{m} \end{bmatrix}}_{\Delta\mathbf{u}} \tag{55}$$

where

$$\begin{aligned}
\mathbf{k}_\mathrm{ss} &= \sum_{i=1}^{a} \mathop{\mathbb{A}}_{e} \mathop{\mathbb{A}}_{e} \Big( \mathbf{M}^{ee}\, w_i\, \epsilon\, g_\mathrm{n} + \epsilon\, \mathbf{G}_e^\mathrm{T}\, w_i\, \mathbf{G}_e \Big) \;, \\
\mathbf{k}_\mathrm{sm} &= \sum_{i=1}^{a} \mathop{\mathbb{A}}_{e} \mathop{\mathbb{A}}_{\hat{e}} \Big( \mathbf{M}^{e\hat{e}}\, w_i\, \epsilon\, g_\mathrm{n} - \epsilon\, \mathbf{G}_e^\mathrm{T}\, w_i\, \mathbf{G}_{\hat{e}} \Big) \;, \\
\mathbf{k}_\mathrm{ms} &= -\sum_{i=1}^{a} \mathop{\mathbb{A}}_{\hat{e}} \mathop{\mathbb{A}}_{e} \Big( \mathbf{M}^{\hat{e}e}\, w_i\, \epsilon\, g_\mathrm{n} + \epsilon\, \mathbf{G}_{\hat{e}}^\mathrm{T}\, w_i\, \mathbf{G}_e \Big) \;, \\
\mathbf{k}_\mathrm{mm} &= -\sum_{i=1}^{a} \mathop{\mathbb{A}}_{\hat{e}} \mathop{\mathbb{A}}_{\hat{e}} \Big( \mathbf{M}^{\hat{e}\hat{e}}\, w_i\, \epsilon\, g_\mathrm{n} + \epsilon\, \mathbf{G}_{\hat{e}}^\mathrm{T}\, w_i\, \mathbf{G}_{\hat{e}} \Big)
\end{aligned} \tag{56}$$

denote the consistent contact stiffness matrices with matrices $\mathbf{M}^{\bullet\bullet}$ and $\mathbf{G}_\bullet$ defined by Eq. (39).

## Appendix B. Adaptive load stepping scheme

In this appendix, an adaptive load stepping scheme used in the 3D numerical examples is described in detail. A prescribed displacement (or an applied external load) is applied incrementally, where in general the load increment – denoted by $\Delta\bar{u}$ – at a load step $k$ is adaptively adjusted based on the Newton iteration count from the previous load step. That is

$$\Delta\bar{u}^k = \alpha^k\, \Delta\bar{u}^{k-1} \;, \qquad \text{with} \quad \Delta\bar{u}^k \in [\Delta\bar{u}_\mathrm{min} \;,\; \Delta\bar{u}_\mathrm{max}] \;, \tag{57}$$

where $\Delta\bar{u}_\mathrm{min}$ and $\Delta\bar{u}_\mathrm{max}$ are user-defined bounds for load increments. Parameter $\alpha$ denotes the step size factor. Accordingly to Magisano et al. [22], it can be defined, for example, as

$$\alpha^k = 1 - \frac{1}{2}\frac{N_{k-1} - N_\mathrm{e}}{N_{k-1} + N_\mathrm{e}} \;. \tag{58}$$

Here $N_{k-1}$ is the number of Newton iterations at the previous load step $(k-1)$, and $N_\mathrm{e}$ is a user-defined parameter, representing the expected (i.e. desired, see cf. [22]) number of Newton iterations per load step.

If increment $\Delta\bar{u}^k$ follows from Eq. (57) exceeds the given bounds, we then take the closest bound ($\Delta\bar{u}_\mathrm{min}$ or $\Delta\bar{u}_\mathrm{max}$) for the current load step. At the first load step, i.e. $k = 1$, the increment $\Delta\bar{u}^k$ is given by a user-defined suggested value $\Delta\bar{u}_\mathrm{suggested}$.

On top of the adaptive increment Eq. (57), in case of divergence of Newton iterations at a load step $k$, the computation is retried (max. 5 times) with 30% of $\Delta\bar{u}^k$ from the previous (failed) attempt. This is to prevent a termination of the simulation due to a too large increment.

## References

[1] T.X. Duong, L. De Lorenzis, R.A. Sauer, A segmentation-free isogeometric extended mortar contact method, Comput. Mech. 63 (2019) 383–407.

[2] Y. Maday, C. Mavriplis, A.T. Patera, Nonconforming mortar element methods: Application to spectral discretizations, in: Domain Decomposition Methods, SIAM, Philadelphia, PA, 1988, pp. 392–418.

[3] M.A. Puso, T.A. Laursen, A mortar segment-to-segment contact method for large deformation solid mechanics, Comput. Methods Appl. Mech. Engrg. 193 (2004) 601–629.
[4] T.J.R. Hughes, J.A. Cottrell, Y. Bazilevs, Isogeometric analysis: CAD, finite elements, NURBS, exact geometry and mesh refinement, Comput. Methods Appl. Mech. Engrg. 194 (2005) 4135–4195.
[5] J. Lu, Isogeometric contact analysis: Geometric basis and formulation for frictionless contact, Comput. Methods Appl. Mech. Engrg. 200 (2011) 726–741.
[6] I. Temizer, P. Wriggers, T. Hughes, Contact treatment in isogeometric analysis with NURBS, Comput. Methods Appl. Mech. Engrg. 200 (2011) 1100–1112.
[7] L. De Lorenzis, I. Temizer, P. Wriggers, G. Zavarise, A large deformation frictional contact formulation using NURBS-based isogeometric analysis, Internat. J. Numer. Methods Engrg. 87 (2011) 1278–1300.
[8] B. Yang, T.A. Laursen, X. Meng, Two dimensional mortar contact methods for large deformation frictional sliding, Internat. J. Numer. Methods Engrg. 62 (2005) 1183–1225.
[9] A. Popp, M. Gitterle, M.W. Gee, W.A. Wall, A dual mortar approach for 3D finite deformation contact with consistent linearization, Internat. J. Numer. Methods Engrg. 83 (2010) 1428–1465.
[10] P. Wriggers, Computational Contact Mechanics, second ed., Springer-Verlag, Berlin Heidelberg, 2006.
[11] T. Cichosz, M. Bischoff, Consistent treatment of boundaries with mortar contact formulations using dual Lagrange multipliers, Comput. Methods Appl. Mech. Engrg. 200 (2011) 1317–1332.
[12] J.-Y. Kim, S.-K. Youn, Isogeometric contact analysis using mortar method, Internat. J. Numer. Methods Engrg. 89 (12) (2012) 1559–1581.
[13] L. De Lorenzis, P. Wriggers, G. Zavarise, A mortar formulation for 3D large deformation contact using NURBS-based isogeometric analysis and the augmented Lagrangian method, Comput. Mech. 49 (2012) 1–20.
[14] I. Temizer, A mixed formulation of mortar-based contact with friction, Comput. Methods Appl. Mech. Engrg. 255 (2013) 183–195.
[15] A. Popp, W.A. Wall, Dual mortar methods for computational contact mechanics – overview and recent developments, GAMM-Mitt. 37 (1) (2014) 66–84.
[16] C.J. Corbett, R.A. Sauer, NURBS-enriched contact finite elements, Comput. Methods Appl. Mech. Engrg. 275 (2014) 55–75.
[17] C.J. Corbett, R.A. Sauer, Three-dimensional isogeometrically enriched finite elements for mixed-mode contact and debonding, Comput. Methods Appl. Mech. Engrg. 284 (2015) 781–806.
[18] K.A. Fischer, P. Wriggers, Frictionless 2D contact formulations for finite deformations based on the mortar method, Comput. Mech. 36 (2005) 226–244.
[19] T.X. Duong, R.A. Sauer, An accurate quadrature technique for the contact boundary in 3D finite element computations, Comput. Mech. 55 (1) (2015) 145–166.
[20] L. De Lorenzis, J. Evans, T. Hughes, A. Reali, Isogeometric collocation: Neumann boundary conditions and contact, Comput. Methods Appl. Mech. Engrg. 284 (2015) 21–54, Isogeometric Analysis Special Issue.
[21] L. De Lorenzis, P. Wriggers, T.J.R. Hughes, Isogeometric contact: A review, GAMM-Mitt. 37 (2014) 85–123.
[22] D. Magisano, L. Leonetti, G. Garcea, How to improve efficiency and robustness of the Newton method in geometrically non-linear structural problem discretized via displacement-based finite elements, Comput. Methods Appl. Mech. Engrg. 313 (2017) 986–1005.
[23] R. Pfefferkorn, S. Bieber, B. Oesterle, M. Bischoff, P. Betsch, Improving efficiency and robustness of enhanced assumed strain elements for nonlinear problems, Internat. J. Numer. Methods Engrg. 122 (8) (2021) 1911–1939.
[24] F. Maurin, F. Greco, S. Dedoncker, W. Desmet, Isogeometric analysis for nonlinear planar Kirchhoff rods: Weighted residual formulation and collocation of the strong form, Comput. Methods Appl. Mech. Engrg. 340 (2018) 1023–1043.
[25] L. Leonetti, F. Liguori, D. Magisano, G. Garcea, An efficient isogeometric solid-shell formulation for geometrically nonlinear analysis of elastic shells, Comput. Methods Appl. Mech. Engrg. 331 (2018) 159–183.
[26] L. Leonetti, D. Magisano, F. Liguori, G. Garcea, An isogeometric formulation of the Koiter's theory for buckling and initial post-buckling analysis of composite shells, Comput. Methods Appl. Mech. Engrg. 337 (2018) 387–410.
[27] L. Leonetti, D. Magisano, A. Madeo, G. Garcea, J. Kiendl, A. Reali, A simplified Kirchhoff–Love large deformation model for elastic shells and its effective isogeometric formulation, Comput. Methods Appl. Mech. Engrg. 354 (2019) 369–396.
[28] L. Leonetti, F.S. Liguori, D. Magisano, J. Kiendl, A. Reali, G. Garcea, A robust penalty coupling of non-matching isogeometric Kirchhoff–Love shell patches in large deformations, Comput. Methods Appl. Mech. Engrg. 371 (2020) 113289.
[29] D. Magisano, L. Leonetti, A. Madeo, G. Garcea, A large rotation finite element analysis of 3D beams by incremental rotation vector and exact strain measure with all the desirable features, Comput. Methods Appl. Mech. Engrg. 361 (2020) 112811.
[30] D. Magisano, L. Leonetti, G. Garcea, Isogeometric analysis of 3D beams for arbitrarily large rotations: Locking-free and path-independent solution without displacement DOFs inside the patch, Comput. Methods Appl. Mech. Engrg. 373 (2021) 113437.
[31] D. Magisano, L. Leonetti, G. Garcea, Unconditional stability in large deformation dynamic analysis of elastic structures with arbitrary nonlinear strain measure and multi-body coupling, Comput. Methods Appl. Mech. Engrg. 393 (2022) 114776.
[32] A. Maghami, F. Shahabian, S.M. Hosseini, Path following techniques for geometrically nonlinear structures based on multi-point methods, Comput. Struct. 208 (2018) 130–142.
[33] D. Magisano, G. Garcea, Sensitivity analysis to geometrical imperfections in shell buckling via a mixed generalized path-following method, Thin-Walled Struct. 170 (2022) 108643.
[34] D. Magisano, A. Corrado, New robust and efficient global iterations for large deformation finite element analysis of beams and shells with material nonlinearity, Comput. Methods Appl. Mech. Engrg. 406 (2023) 115900.
[35] J.C. Simo, P. Wriggers, R.L. Taylor, A perturbed Lagrangian formulation for the finite element solution of contact problems, Comput. Methods Appl. Mech. Engrg. 50 (2) (1985) 163–180.

[36] R.A. Sauer, L. De Lorenzis, A computational contact formulation based on surface potentials, Comput. Methods Appl. Mech. Engrg. 253 (2013) 369–395.
[37] R.W. Ogden, Non-Linear Elastic Deformations, Dover Edition, Mineola, 1987.
[38] A. del Toro Llorens, J. Kiendl, An isogeometric finite element-boundary element approach for the vibration analysis of submerged thin-walled structures, Comput. Struct. 256 (2021) 106636.
[39] K.L. Johnson, Contact Mechanics, Cambridge University Press, 1985.
[40] R. Sevilla, S. Fernández-Méndez, A. Huerta, Nurbs-enhanced finite element method (nefem), Internat. J. Numer. Methods Engrg. 76 (1) (2008) 56–83.
[41] J. Kiendl, K.-U. Bletzinger, J. Linhard, R. Wüchner, Isogeometric shell analysis with Kirchhoff–Love elements, Comput. Methods Appl. Mech. Engrg. 198 (2009) 3902–3914.
[42] R.A. Sauer, T.X. Duong, C.J. Corbett, A computational formulation for constrained solid and liquid membranes considering isogeometric finite elements, Comput. Methods Appl. Mech. Engrg. 271 (2014) 48–68.
[43] T.X. Duong, F. Roohbakhshan, R.A. Sauer, A new rotation-free isogeometric thin shell formulation and a corresponding continuity constraint for patch boundaries, Comput. Methods Appl. Mech. Engrg. 316 (2017) 43–83.
[44] C. Zimmermann, D. Toshniwal, C.M. Landis, T.J. Hughes, K.K. Mandadapu, R.A. Sauer, An isogeometric finite element formulation for phase transitions on deforming surfaces, Comput. Methods Appl. Mech. Engrg. 351 (2019) 441–477.